# RESEARCH ARTICLE SUMMARY

## CELL BIOLOGY

# Nuclear pores dilate and constrict in cellulo

Christian E. Zimmerli†, Matteo Allegretti†, Vasileios Rantos, Sara K. Goetz, Agnieszka Obarska-Kosinska, Ievgeniia Zagoriy, Aliaksandr Halavatyi, Gerhard Hummer, Julia Mahamid, Jan Kosinski*, Martin Beck*

**INTRODUCTION:** The nucleus harbors and protects the genetic information in eukaryotes. It is surrounded by the nuclear envelope, which separates the nucleoplasm from the cytosol. The double-membrane system of the nuclear envelope is physically connected to the cytoskeleton and chromatin on either side. It senses and signals mechanical stimuli. Nuclear pore complexes (NPCs) mediate nucleocytoplasmic exchange. They fuse the inner and outer nuclear membranes of the nuclear envelope to form an aqueous central channel. Their intricate cylindrical architecture consists of ~30 nucleoporins. The nucleoporin scaffold embraces the membrane fusion topology in a highly dynamic fashion. Variations in NPC diameter have been reported, but the physiological circumstances and the molecular details remain unknown.

**RATIONALE:** To investigate the dynamics of NPC conformation in vivo, we structurally analyzed NPCs in *Schizosaccharomyces pombe* cells. We used cryo–electron tomography with subsequent subtomogram averaging to quantify the diameter of NPCs in cells exposed to different stress stimuli. We found a dilated NPC scaffold in exponentially growing cells that constricted under conditions of energy depletion and hyperosmotic shock. Structural analysis in combination with integrative structural modeling revealed that the NPC scaffold underwent large-scale movements and bending during constriction. Thereby, the volume of the central channel was lessened to about one-half. Reduced nucleocytoplasmic diffusion was apparent. Scaffold nucleoporins do not have any known motor activity that would allow them to exert forces. Thus, it appears likely that the observed dynamics of the diameter of the NPC were the result of forces that are laterally applied within the nuclear envelope. Under conditions of both energy depletion and hyper-osmotic shock, cellular and nuclear volumes were reduced such that nuclear shrinkage led to an excess of nuclear membranes. We therefore hypothesized that the NPC scaffold is mechanosensitive. We surmised that a reduction of nuclear envelope membrane tension resulted in a consequent NPC constriction into a conformational ground state.

**RESULTS:** We outline several predictions of a conceptual model in which nuclear envelope membrane tension regulates NPC diameter. In such a scenario, nuclear volume and NPC diameter should be dependent on each other. The rigidity of the NPC scaffold should counteract its dilation. On the basis of membrane elastic theory, we predicted that osmotic pressure in the nuclear envelope lumen and membrane tension in the nuclear envelope act equivalently. As a consequence, the distance between the inner and outer nuclear membranes should grow linearly with both. We set out to test those predictions experimentally. We found that nuclear shrinkage correlated with NPC constriction. Recovery experiments established that this behavior was reversible. Constricted NPCs dilated when shifted back to normal medium. Nuclear volumes recovered, and cells remained viable. In exponentially growing cells, genetic perturbation of the NPC scaffold resulted in further dilation. We segmented the inner and outer nuclear membranes in cryo–electron tomograms and quantified their distance. As expected, the diameter of the NPC directly correlated with the distance between the inner and outer nuclear membranes.

**CONCLUSION:** Our data strongly suggest that the NPC scaffold is mechanosensitive and that membrane tension regulates its diameter. The data link the conformation of the NPC to the mechanical status of the nuclear envelope. This finding has implications for various cellular processes during which the nucleus may be exposed to mechanical forces. This includes cell differentiation and migration, nuclear envelope maintenance in mechanically active tissues, the import of very large cargos such as viral capsids, metastasis, and changing osmotic conditions. Under such conditions, nuclear envelope membrane tension will change globally or locally. The resulting changes in the diameter of the NPC may have functional consequences that remain to be investigated further in the future. ∎
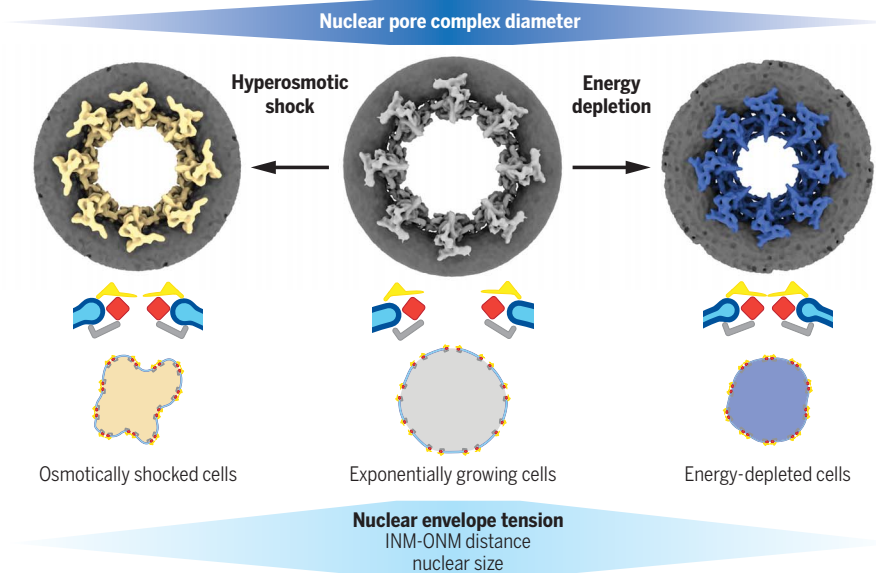


**NPCs constrict under conditions of cellular energy depletion and hyperosmotic shock.** Cryo–electron microscopy maps of different NPC conformations are shown isosurface rendered as seen from the cytosol in exponentially growing (light gray), hyperosmotically shocked (yellow), and energy-depleted cells (blue) (top). Nuclear membranes are shown in dark gray. Cartoons indicate the respective conformational changes. Upon exposure to hyperosmotic shock and energy depletion, NPCs constrict to smaller central channel diameters. The nuclear volume is decreased, and the distance between the inner and outer nuclear membranes is reduced (bottom), which is indicative of a loss of nuclear envelope membrane tension. INM, inner nuclear membrane; ONM, outer nuclear membrane.

**READ THE FULL ARTICLE AT**
https://doi.org/10.1126/science.abd9776

<div style="background:red">RESEARCH ARTICLE</div>

## CELL BIOLOGY

# Nuclear pores dilate and constrict in cellulo

Christian E. Zimmerli[1,2,3]†, Matteo Allegretti[1,3]†, Vasileios Rantos[4,5], Sara K. Goetz[1,2],
Agnieszka Obarska-Kosinska[3,5], Ievgeniia Zagoriy[1], Aliaksandr Halavatyi[6], Gerhard Hummer[7,8],
Julia Mahamid[1], Jan Kosinski[1,4,5]*, Martin Beck[1,3]*

In eukaryotic cells, nuclear pore complexes (NPCs) fuse the inner and outer nuclear membranes and mediate nucleocytoplasmic exchange. They are made of 30 different nucleoporins and form a cylindrical architecture around an aqueous central channel. This architecture is highly dynamic in space and time. Variations in NPC diameter have been reported, but the physiological circumstances and the molecular details remain unknown. Here, we combined cryo–electron tomography with integrative structural modeling to capture a molecular movie of the respective large-scale conformational changes in cellulo. Although NPCs of exponentially growing cells adopted a dilated conformation, they reversibly constricted upon cellular energy depletion or conditions of hypertonic osmotic stress. Our data point to a model where the nuclear envelope membrane tension is linked to the conformation of the NPC.

N uclear pore complexes (NPCs) bridge the nuclear envelope (NE) and facilitate nucleocytoplasmic transport. Across the eukaryotic kingdom, ~30 different genes encode for NPC components, termed nucleoporins (Nups). Although specialized Nups have been identified in many species, extensive biochemical and structural studies have led to the consensus that the core scaffold inventory is conserved. It consists of several Nup subcomplexes that come together in multiple copies to form an assembly of eight asymmetric units, called spokes, that are arranged in a rotationally symmetric fashion (*1*). The Y-complex (also called the Nup107 complex) is the major component of the outer rings [the nuclear ring (NR) and the cytoplasmic ring (CR)], which are placed distally into the nuclear and cytoplasmic compartments. The inner ring complex scaffolds the inner ring [(IR) also called the spoke ring] that resides at the fusion plane of the nuclear membranes. It consists of the scaffold Nups 35, 155, 188, and 192 as well as the Nsp1 complex. The IR forms a central channel lined with phenylalanine-glycine (FG) repeats containing Nups that interact with cargo complexes. The Nup159 complex (also called the P-complex) asymmetrically associ-

ates with the Y-complex of the CR and mediates mRNA export. Despite these common features of quaternary structure, in situ structural biology studies have revealed that the higher-order assembly is variable across the eukaryotic kingdom (*1*, *2*).

NPC architecture is conformationally highly dynamic, and variations in NPC diameter have been observed in various species and using different methods (*3–7*). Dilated states have been observed in intact human cells (*3*, *8*, *9*), contrasting with the constricted state in semipurified NPCs (*10–12*). It has been shown that dilation is part of the NPC assembly process (*13*, *14*). However, it remains controversial whether NPC dilation and constriction play a role during active nuclear transport (*15*) and whether the dilation is required to open up peripheral channels for the import of inner nuclear membrane (INM) proteins (*16–18*). It has been argued that the constricted state may be a result of purification (*4*, *8*). It is difficult to conceive that such large-scale conformational changes can occur on similar time scales as individual transport events (*19*, *20*), which would be the essence of a physical gate. Nevertheless, several cues that potentially could affect NPC diameter have been suggested, such as exposure to mechanical stress, mutated forms of importin β, varying Ca²⁺ concentrations, or exposure to hexanediol (*7*, *21–26*). The biological relevance of these cues remains elusive because the analysis of NPC architecture under physiological conditions is experimentally very challenging. These previous studies did not explore NPC dilation and constriction and its functional cause and consequences within intact cellular environments, nor did they structurally analyze the conformational changes of nuclear pores in high molecular detail.

Here, we demonstrate that *Schizosaccharomyces pombe* NPCs (SpNPCs) constrict in living cells

under conditions of energy depletion (ED) or hyperosmotic shock (OS), which is concomitant with a reduction of NE membrane tension. Using in cellulo cryo–electron microscopy (cryo-EM) and integrative structural modeling, we captured a molecular movie of NPC constriction. Our dynamic structural model suggests large-scale conformational changes that occur by movements of the spokes with respect to each other but largely preserve the arrangement of individual subcomplexes. Previous structural models obtained from isolated NEs (*10–12*, *27–29*) thereby represent the most constricted NPC state.

## In cellulo cryo-EM map of the SpNPC

To study NPC architecture and function in cellulo at the best possible resolution and structural preservation, we explored various genetically tractable model organisms for their compatibility with cryo–focused ion beam (cryo-FIB) specimen thinning, cryo–electron tomography (cryo-ET), and subtomogram averaging (STA). *Saccharomyces cerevisiae* cells were compatible with high-throughput generation of cryo-lamellae and acquisition of tomograms. STA of their NPCs resulted in moderately resolved structures (*4*). By contrast, a larger set of cryo-tomograms from *Chaetomium thermophilum* cells did not yield any meaningful averages, possibly because their NPCs displayed a very large structural variability. We therefore chose to work with *S. pombe* cells that are small enough for thorough vitrification; offer a superior geometry for FIB milling compared with *C. thermophilum*, with the advantage of covering multiple cells; and, compared with *S. cerevisiae*, have a higher number of NEs and NPCs per individual cryo-lamella and tomogram, leading to increased data throughput (fig. S1).

To obtain a high-quality cryo-EM map of SpNPCs, we prepared cryo-FIB–milled lamellae of exponentially growing *S. pombe* cells and acquired 178 tomograms from which we extracted 726 NPCs. Subsequent STA resulted in an in cellulo NPC average of very high quality in both visible features and resolution (Fig. 1 and figs. S2 and S3). Systematic fitting of the *S. pombe* IR asymmetric unit model, built based on the *S. cerevisiae* NPC, resulted in precisely one highly significant fit, as expected (figs. S4A and S5A and Materials and methods). The subsequent refinement with integrative modeling led to a structural model that explains most of the observed EM density in the IR (Fig. 1B, fig. S5B, and movie S1). The IR architecture appears reminiscent to NPC structures of other eukaryotes (fig. S6), further corroborating its evolutionary conservation (*2*, *30*) (see table S1 for nomenclature of Nups across different species). Systematic fitting revealed that the NR of the SpNPC is composed of two concentric Y-complex rings (Fig. 1A,

¹Structural and Computational Biology Unit, European Molecular Biology Laboratory (EMBL), 69117 Heidelberg, Germany. ²Collaboration for joint PhD degree between EMBL and Heidelberg University, Faculty of Biosciences, 69120 Heidelberg, Germany. ³Department of Molecular Sociology, Max Planck Institute of Biophysics, 60438 Frankfurt am Main, Germany. ⁴Centre for Structural Systems Biology (CSSB), 22607 Hamburg, Germany. ⁵EMBL Hamburg, 22607 Hamburg, Germany. ⁶Advanced Light Microscopy Facility, EMBL, 69117 Heidelberg, Germany. ⁷Department of Theoretical Biophysics, Max Planck Institute of Biophysics, 60438 Frankfurt am Main, Germany. ⁸Institute of Biophysics, Goethe University Frankfurt, 60438 Frankfurt am Main, Germany.
*Corresponding author. Email: jan.kosinski@embl.de (J.K.); martin.beck@biophys.mpg.de (M.B.)
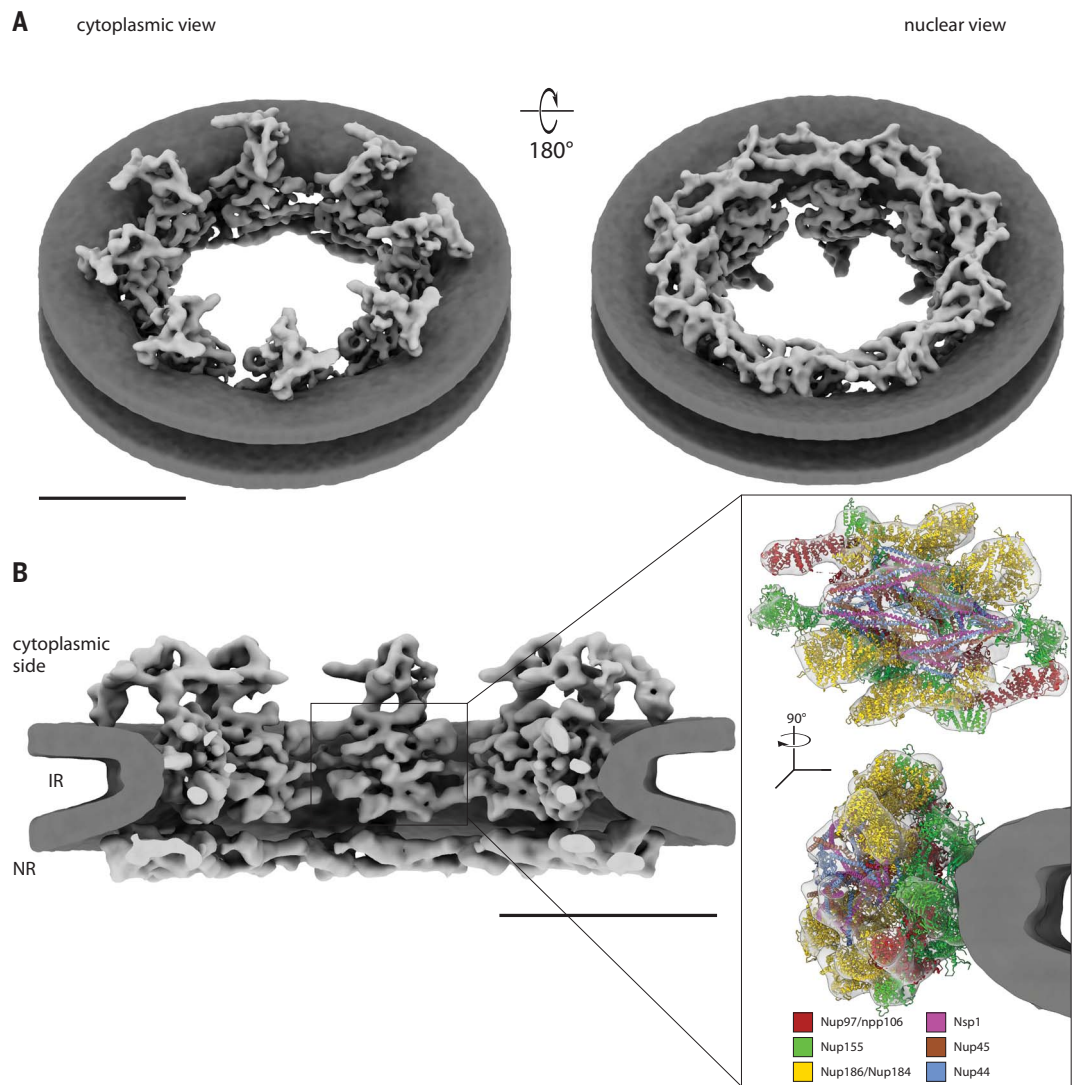†These authors contributed equally to this work.

**Fig. 1. In cellulo cryo-EM map of the SpNPC.** (**A**) Isosurface rendered views of the SpNPC eightfold assembly as seen from the cytoplasm (left) and the nucleoplasm (right) (with membranes in dark gray and protein in light gray). Note, the eightfold symmetric assembly represents an artificial NPC conformation; within living cells, NPCs adopt more-flexible conformations deviating from a perfect circle. Although the cytoplasmic view (left) reveals eight disconnected protein entities instead of a CR, the nuclear view (right) shows two concentric nuclear Y-complex rings. Scale bar, 50 nm. (**B**) Same as (A) but shown as a cutaway view. Although the asymmetric curvature of the nuclear membranes and the arrangement of the cytoplasmic side is unprecedented in other species, the IR architecture is highly conserved, as highlighted in the inset (see also fig. S6). Scale bar, 50 nm. The inset shows one individual asymmetric IR unit map as obtained during STA (see Materials and methods); the density threshold is chosen at a level comparable to the entire eightfold assembly. In the side view (inset, below), the membrane is shown for reference. Fitting of the IR Nup homology models explains most of the observed electron optical density.



A cytoplasmic view · nuclear view · 180°

B cytoplasmic side · IR · NR · 90°

Nup97/npp106 · Nsp1 · Nup155 · Nup45 · Nup186/Nup184 · Nup44

fig. S4B, and movie S1) as in vertebrates and algae but as opposed to the single ring observed in *S. cerevisiae* (fig. S3A) (*4*, *11*, *31*). Integrative modeling of the entire Y-complex in the NR revealed a Y-complex architecture with the typical head-to-tail oligomerization (Fig. 2A). It recapitulates the domain orientations and interactions known from other species. However, *S. pombe* Y-complex Nups do localize to the NR, in contrast to previous proposals (*32*).

Closer inspection of the cytoplasmic side of the cryo-EM map revealed an unanticipated architectural outline—it did not form an apparent ring. Instead, we observed eight spatially separated entities (Fig. 1A), which serve as anchor points for the mRNA export platform (*4*, *33*), the Nup159 complex (Fig. 2B). Although the dynein-arm characteristic for the *S. cerevisiae* NPC (*34*) is lacking, the Nup159 complex resembles its *S. cerevisiae* counterpart in shape (fig. S7A). Systematic fitting and subsequent refinement with integrative

modeling revealed that only a single Y-complex vertex fits into the density observed at the cytoplasmic side (Fig. 2B, fig. S4C, and movie S1). The density potentially accounting for Nup107 and SpNup131-SpNup132 was missing (figs. S4D and S7B) and could not be recovered by local refinement (fig. S7C). To independently confirm the identity of the observed vertex-like density, we analyzed *nup37Δ* and *nup37Δ-ely5Δ* strains. The binding of both Nup37 and Ely5 to Nup120 has been shown previously in vitro (*35*, *36*), and, as expected, density was missing in the respective positions of all Y-complexes (Fig. 2, C and D, and figs. S8 and S9). A density that could accommodate the Ely5 homology model was missing also in the cytoplasmic Y-complex, suggesting that Ely5 is present in *S. pombe* at both sides, unlike its human counterpart Elys (*11*, *37*) (Fig. 2D and movie S1). Otherwise, the NPC architecture remained mostly unchanged, despite some increased flexibility in

the Nup120 arm of the outer nuclear Y-complex pointing to a decreased NR stability under knockout conditions. These results independently identify the cytoplasmic structure as bona fide Y-complex vertex but lacking the EM density beyond the edge of SpNup189C. This is consistent with previous work suggesting a split of the SpNup189C-Nup107 interface (*32*, *38*). Alternatively, this observation may be explained by flexibility, although hinges within the Y-complex were identified at different locations (*10*, *39*).

## ED is concomitant with a constriction of the central channel

Previous cryo-EM structures of NPCs obtained from isolated NEs (*10–12*, *27–29*) or by detergent extraction (*40*) had a smaller diameter compared with those obtained from intact cells (*3*, *4*, *31*, *41*). We therefore hypothesized that NPC diameter may depend on the biochemical energy level, which is diminished

**Fig. 2. Architecture of SpNPC outer rings.** (**A**) Systematic fitting and integrative modeling of all *S. pombe* Y-complex Nups reveal a head-to-tail arrangement with two concentric Y-complex rings on the nuclear side of the SpNPC, as in the human NPC (*11*). The cryo-EM map of a NR segment is shown rendered as an isosurface in transparent light gray. The adjacent inner Y-complexes are shown in gray, and the outer Y-complexes are shown in orange. The homology models of SpNup131 and SpNup132 fit to the Y-complex tail region equally well, rendering these two proteins indistinguishable by our approach. (**B**) Integrative model of the cytoplasmic protein entities. The fit of the Y-complex vertex explains most of the observed density. The mRNA export platform as identified in (*4, 33*) is segmented in yellow. (**C**) The *nup37Δ* cryo-EM map is shown in blue (threshold: 0.1) and overlaid with the difference map (yellow; threshold: 0.175) of the WT and *nup37Δ* maps, both filtered to 27 Å. The missing density in the long arm of the Y-vertex coincides with the position of Nup37 (indicated by the dark red dagger symbol) in the Y-complex vertex (dark gray) (see also fig. S8). (**D**) The *nup37Δ-ely5Δ* double knockout map (blue; threshold: 0.08) overlaid with the corresponding difference map (yellow; threshold: 0.188) comparing the WT and double knockout map at 34 Å. Differences are apparent at the location of both Nup37 (dark red dagger symbol) and Ely5 (light red number symbol) with respect to the fitted Y-complex model (dark gray) (see also fig. S9).
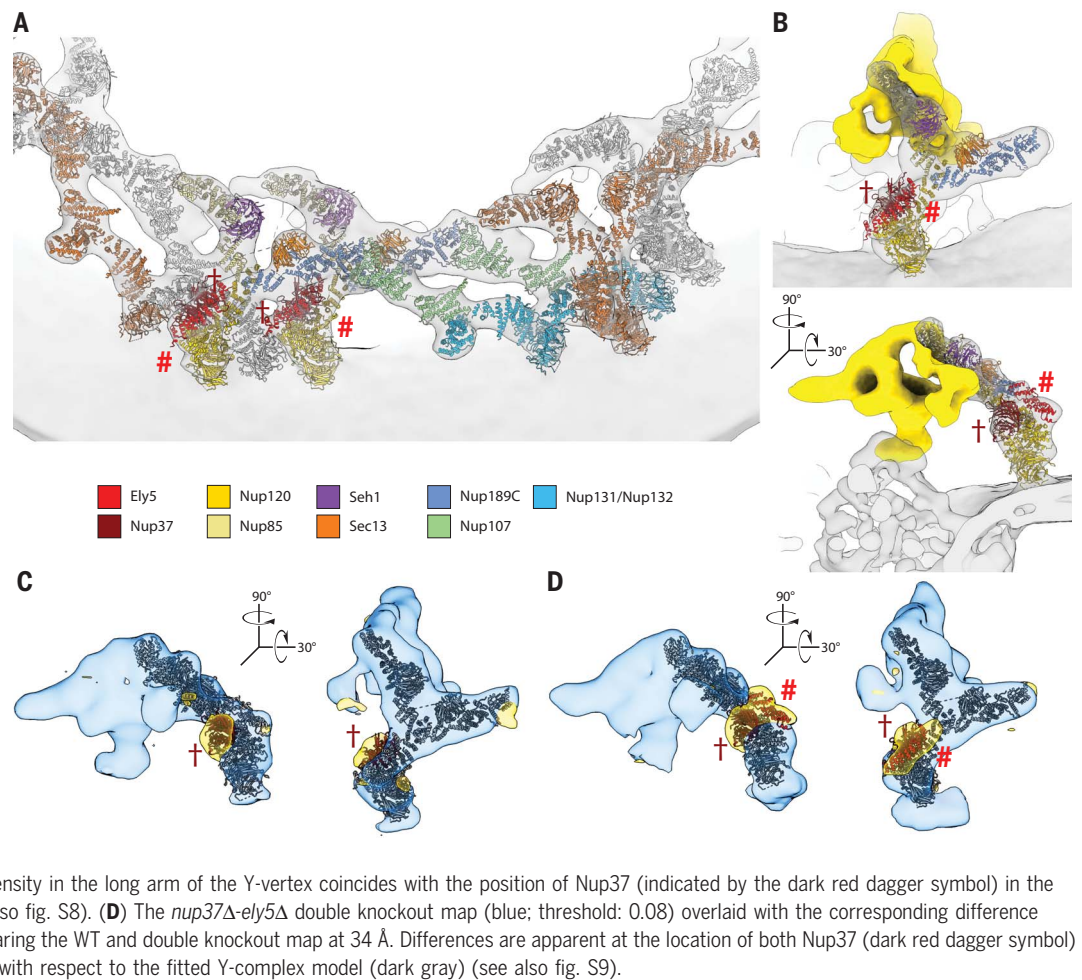
in preparations of isolated NEs or NPCs but may also be reduced within intact cells—e.g., during stress conditions. We first set out to analyze NPCs in *S. pombe* cells under conditions of ED, namely after 1 h of exposure to nonhydrolyzable 2-deoxy-glucose in combination with the respiratory chain inhibitor antimycin A, as previously established (*42*) (see Materials and methods). Recovery experiments demonstrated the viability of cells exposed to ED, and the subcellular architecture of the respective cells remained intact, as apparent by cryo-ET (fig. S10). Cells of various organisms including *S. pombe* show a rapid shut down of active nuclear transport and mRNA export when depleted of adenosine 5′-triphosphate (ATP) because of a concomitant reduction of guanosine 5′-triphosphate (GTP) levels, which leads to the loss of the nucleocytoplasmic RanGTP-RanGDP (GDP, guanosine diphosphate) gradient (*43–46*). To confirm a loss of active nucleocytoplasmic transport under ED conditions, we used live-cell imaging of *S. pombe* cells expressing a green fluorescent protein (GFP) variant tagged with a nuclear localization signal (NLS) or nuclear export signal (NES) on its N and C terminus

(NLS-GFP-NLS or NES-GFP-NES), which show a nearly exclusive nuclear or cytoplasmic localization under control conditions (fig. S11, A to D). After 30 min of ED, most of the NLS-GFP-NLS localized to the cytoplasm, whereas NES-GFP-NES equilibrated into the nucleus (fig. S11, A to D). This was reverted in the vast majority of cells when recovered in glucose control medium (fig. S11, E to G), thus underlining their viability.

We analyzed 292 NPCs structurally by STA under these conditions and found a considerable constriction of the central channel diameter. However, the averages appeared blurred, and manual inspection of the data indicated a large variation of diameters. To generate a conformationally more-homogeneous ensemble, we manually assigned the NPCs from the ED dataset into two classes with central channel diameters of <50 nm and >50 nm and refined them separately (corresponding to 533 and 1012 subunits, respectively) (Fig. 3 and fig. S12, A to C). Both conformations of the ED state showed a smaller NPC diameter compared with the conformation observed in NPCs of exponentially growing cells, from here on referred to as control conditions. The inter-

mediate conformation was ~65-nm wide at the IR compared with ~70 nm under control conditions, whereas the most-constricted conformation showed a diameter of ~50 nm, comparable to the diameter observed in isolated NEs (*10–12, 27–29*).

To better understand how NPCs accommodate such massive conformational changes on the molecular level, we systematically fitted individual subcomplexes (fig. S13) and built structural models of the three different diameter states on the basis of the cryo-EM maps (fig. S14) using integrative modeling (fig. S5B). Both systematic fitting and integrative modeling showed that the relevant subunits are present in the control state and the ED states. At the cytoplasmic side and the NR, changes in the curvature of the Y-complexes and inward bending of the mRNA export platform toward the center of the pore were apparent (movies S4 to S6). By contrast, the central channel constriction of the IR is more elaborate and mediated by a lateral displacement of the eight spokes that move as independent entities to constrict or dilate the IR (fig. S14 and movies S4 to S6). In the control state, ~3- to 4-nm-wide gaps are formed in-between the neighboring

**cytoplasmic view**
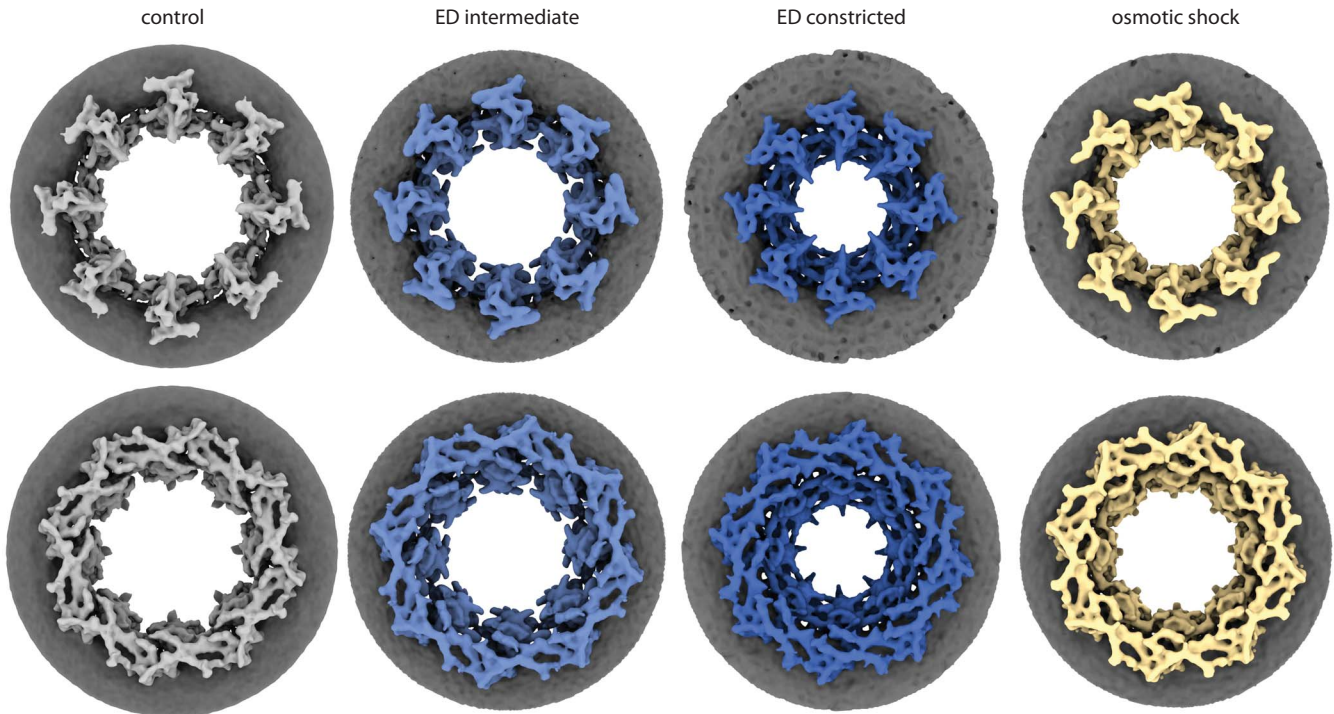


**nuclear view**

**Fig. 3. NPCs constrict during ED and OS.** Cytoplasmic and nuclear views of NPC conformations during control, intermediate, and fully constricted ED and OS conditions, illustrating the overall conformational change leading to a central channel diameter constriction from ~70 to <50 nm. The cytoplasmic and IR spokes move as individual entities and contribute the most to the central channel diameter change, whereas the NR constricts to a lesser extent. Scale bar, 50 nm.

spokes. By contrast, in the constricted state, the spokes form extensive contacts (Fig. 4, A and B) equivalent to those in the previously published structures of the human NPC in isolated NEs (12). It is plausible that such opening and closing of peripheral gaps may regulate the translocation of INM proteins (16–18). Notably, under conditions of ED, additional density is arching out into the lumen of the NE (Fig. 4, A, B, and D), contrasting control conditions. It has been previously proposed that such luminal structures are formed by Pom152 (ScPom152 or HsGP210) (47, 48). In terms of their shape, the observed arches are reminiscent of those observed in isolated *Xenopus laevis* NEs (28). Our data imply that the luminal ring conformation becomes more prominent upon constriction. Whether this has any mechanical benefits to keep NPCs separated (28), or limit the maximal dilation or constriction, remains unclear.

### Hyperosmotic shock results in constriction of the central channel

We noticed that ED was concomitant with a substantial reduction of nuclear size and speculated that it could be functionally related to NPC constriction. To test this hypothesis, we triggered nuclear shrinkage independently

from ED. We caused a OS by exposing cells to 1.2 M sorbitol. This treatment leads to a pronounced loss of cellular and nuclear volume (49). A cryo-EM map from 200 NPCs (Fig. 3; Fig. 4, C and D; and fig. S15A) revealed a strongly constricted conformation. Individual structural features, such as tight lateral packing of IR segments and arching out of the luminal domain, were very similar to those observed with ED, with one notable exception: The N-terminal domain of Nup107 was now clearly resolved at the cytoplasmic side, with the expected angle of engagement of the Nup189C-Nup107 interface (fig. S15B) and consistent with the previously described hinge of the Y-complex (39). This observation may be interpreted as either compositional rearrangement or reduced flexibility. Notably, our findings emphasize that nuclear shrinkage correlates with NPC constriction independent of ED.

### Passive nucleocytoplasmic transport is reduced under ED and OS conditions

To assess whether the NPC constriction under OS and ED conditions correlates with reduction of passive transport across the NE, we performed fluorescence recovery after photobleaching (FRAP) experiments of nuclei at

different time points after ED in cells expressing freely diffusing GFP, as compared with control conditions (Fig. 5, A and B, and fig. S16, A and B) (see Materials and methods). GFP diffusion rates into the nucleus were significantly decreased upon ED (Fig. 5C), contrasting a minor, negligible effect observed within the cytoplasm (fig. S16C). Recovery experiments restored the initially observed diffusion rates (fig. S16D). Under OS conditions, nucleocytoplasmic diffusion decreased to a much lesser extent (Fig. 5, D to F). In contrast to ED, cytoplasmic diffusion also decreased (fig. S16, E to I) in line with previous reports, which demonstrate that OS strongly increases cellular crowding (42, 50). Because ED also leads to a considerable cellular reorganization, including solidification of the cytoplasm, pH-shift, and water loss (42, 51–53), it is difficult to disentangle whether the observed reduction in passive exchange rates is a direct consequence of NPC constriction. How exactly NPC constriction affects the passive and active transport of different types of cargos remains to be determined.

### NE tension regulates NPC diameter

Scaffold Nups do not have any known motor activity that would allow them to exert forces.
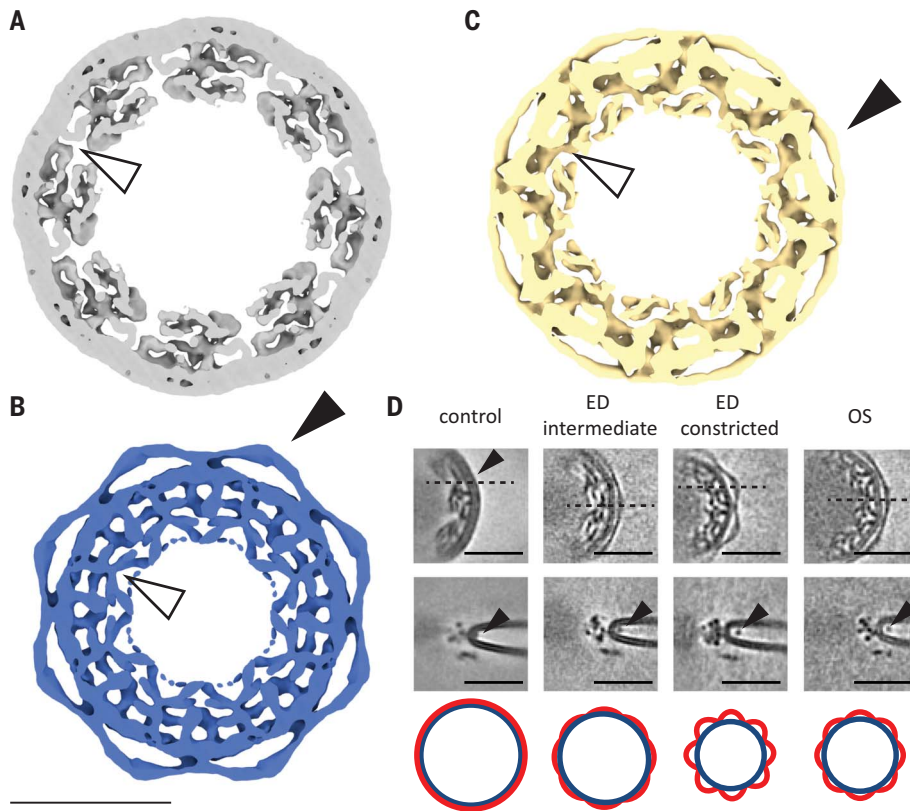
**Fig. 4. Conformational changes of the luminal ring and IR during NPC constriction.** (**A** to **C**) Central slice through an isosurface representation of NPCs under control (A), most-constricted ED (B), and OS (C) conditions. Under control conditions, IR spokes are clearly separated by 3- to 6-nm gaps and form extensive contacts during NPC constriction (white arrowheads). Luminal densities (black arrowheads) are arching into the NE lumen during NPC constriction. Scale bar, 50 nm. (**D**) Horizontal slices through the IR of cryo-EM maps of control, intermediate, and most-constricted ED and OS conditions (left to right). NPCs reveal the appearance of an arch-like density (black arrowheads) during constriction, likely corresponding to the C-terminal domains of Pom152, whereas the N terminus is attached to the NPC (*48*), which is consistent with previous work on isolated NEs (*28*). Dashed lines indicate the position of the orthogonal slices (below) with the luminal density marked by arrowheads. The cartoons (bottom) indicate how a constriction of the nuclear pore membrane (blue) leads to an arching out of Pom152 C-terminal luminal domains (red), whereas the N termini remain closely attached to the NE. Scale bar, 50 nm; slice thickness, 1.35 to 1.38 nm. In control conditions, the luminal densities are directly proximal to the NPC and thus not easily discernible from the membrane.

Thus, it appears more likely that NPC diameter changes result from mechanical forces that are applied externally. Membrane tension, as the energetic cost to expand the membrane area, results in lateral forces within the NE. We hypothesized that the rigidity of the NPC scaffold counteracts lateral forces imposed by NE tension. In such a scenario, an excess of membrane induced by nuclear shrinkage during OS and ED conditions would reduce tension and result in NPC constriction. This would be consistent with the fact that the most constricted conformation of NPCs is observed in isolated NEs where no mechanical forces act on the scaffold (*10–12*, *27–29*, *40*).

A model in which membrane tension pulls apart the NPC scaffold to dilate the central channel makes several predictions: (i) Perturbation of the structural integrity of the NPC scaffold should cause NPC dilation; (ii) the more rigid parts of the *S. pombe* scaffold, such as the NR, should be less responsive to lateral forces and constrict less compared with the more fragile part, namely the IR and cytoplasmic side, which in *S. pombe* does not form a rigid ring; (iii) nuclear shrinkage and deformation that are indicative of reduced NE tension (*54*, *55*) should coincide with NPC constriction; (iv) a reduced distance between the INM and outer nuclear membrane (ONM) should directly correlate with NPC constriction; and (v) recovery of nuclear volume, shape, and INM-ONM distance should restore the initial, dilated NPC diameters. Regarding the latter two predictions, it had been proposed

that a reduced distance between the INM and ONM is indicative of reduced pressure within the NE lumen (*56*). Using membrane elastic theory, we show that osmotic pressure in the NE lumen and membrane tension in the NE act equivalently (supplementary text) and that the INM-ONM distance grows linearly with both.

To test predictions (i) and (ii), we systematically measured the NPC diameter across all investigated conditions based on centroids of opposite asymmetric subunits as obtained by STA (Fig. 6A and fig. S17, A to F) (see Materials and methods). Knockouts of the scaffold Nups Ely5 and Nup37 caused a dilation of the scaffold (Fig. 6A). We quantified the diameters of each ring under NPC-constricting conditions and found that although all three rings constrict significantly, the conformational changes are considerably smaller at the NR that has a more elaborate scaffold as opposed to the cytoplasmic side that does not form a closed ring (Fig. 6B and movies S4 to S6). These findings are consistent with our model.

To test a relationship of nuclear shrinkage and deformation with NPC diameter [prediction (iii)], we quantified nuclear volume and shape on the basis of three-dimensional (3D) reconstructions of nuclear membranes from confocal fluorescence light microscopy z-stacks and segmentation of nuclear membranes in cryo–electron tomograms for ED- and OS-treated cells. The nuclear volume was reduced in both cases and was reverted when cells were recovered from ED (Fig. 7, A to D, and fig. S18A). Nuclear shrinkage should lead to an excess of nuclear membranes if the total nuclear surface area remains constant, which we verified by quantification of the number of NPCs per NE surface in electron tomograms (Fig. 7E). Under conditions of OS, nuclei were also considerably deformed (Fig. 7, B, F, and G, and fig. S18, B and C). Thus, nuclear shrinkage is concomitant with NPC constriction in both OS and ED conditions (Fig. 7H). Nuclear deformation coincides with NPC constriction during OS but is less apparent during ED (Fig. 7, A and I, and fig. S18, C and D), which we attribute to the missing energy-dependent nuclear deformation forces derived from microtubules (*57*, *58*). Alternatively, the more consistent response of cells to OS compared with ED conditions may explain this effect.

Next, we investigated a relationship between the distance between the INM and ONM and the NPC diameter [prediction (iv); supplementary text]. Under both ED and OS conditions, the average INM-ONM distance was reduced from 22.6 nm in control cells to 15.8 and 19.5 nm, respectively, and reverted to control levels upon recovery from OS, further underlining a loss of NE tension (*56*, *59*) (Fig. 7J) and in agreement with our theoretical model (supplementary text). On the level
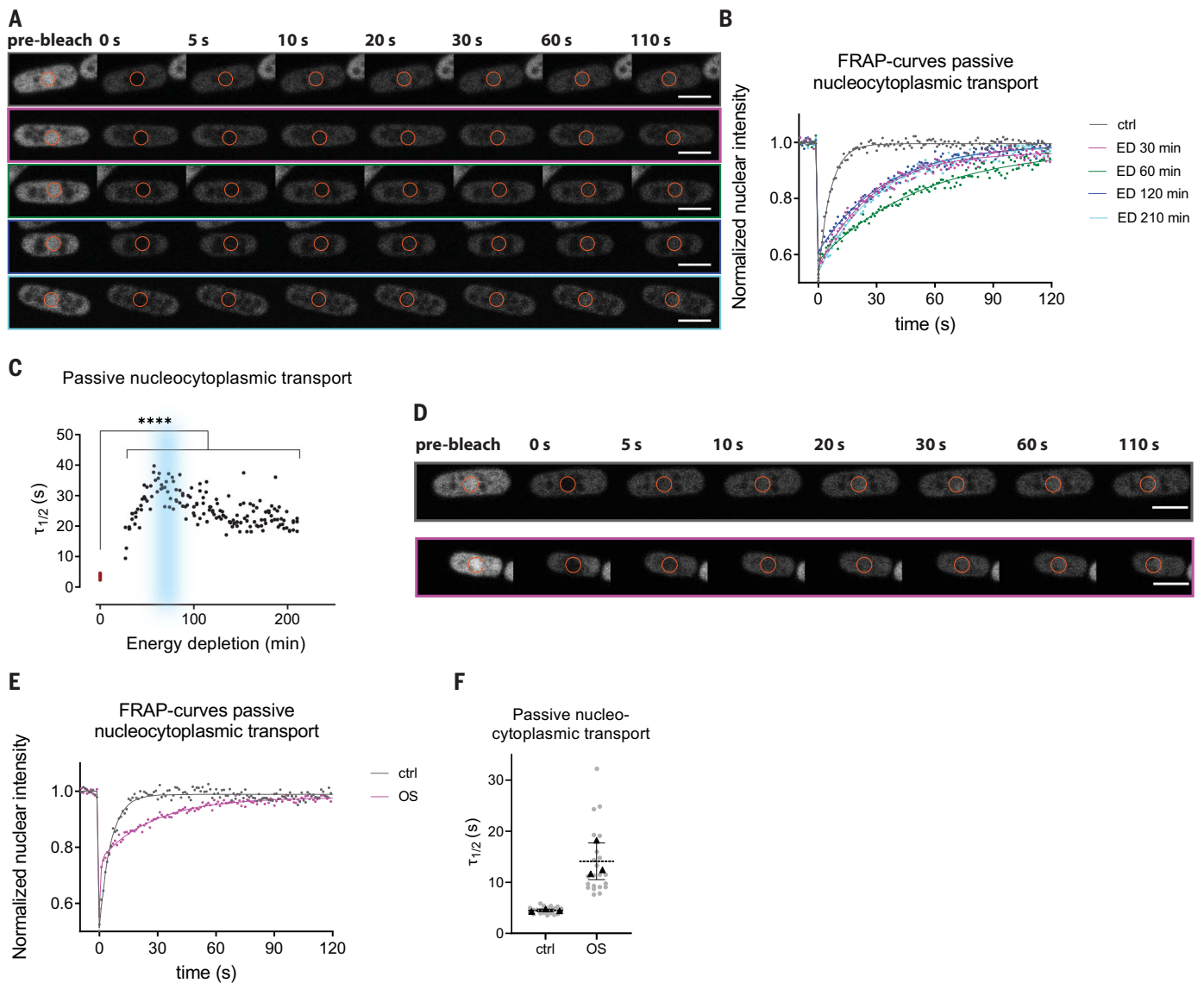
**Fig. 5. FRAP experiments and quantification of passive nucleocytoplasmic transport during ED and OS.** (**A**) Representative FRAP images from time series of passive nucleocytoplasmic diffusion acquired during control conditions (gray) and at 30 min (purple), 60 min (green), 120 min (dark blue), and 210 min (cyan) after ED (from top). Scale bars, 5 μm. (**B**) FRAP curves corresponding to time series in (A). ctrl, control. (**C**) FRAP recovery half-life times of nuclear signal from freely diffusing GFP at various time points during ED are significantly longer compared with control conditions (red dots). Passive transport of free GFP reaches a minimum after ~1 hour of ED and subsequently recovers slightly. The blue area shows the time point at which cryo-EM grids were prepared for structural analysis of ED NPCs. Data are from three experiments, and triangles indicate means of individual replicates ($n = 24$ cells in control and $n = 154$ cells in ED time series). Unpaired $t$ test; ****$P < 0.0001$. (**D** and **E**) Representative snapshots of passive nucleocytoplasmic transport in control (top) and OS conditions (bottom) (D) and corresponding FRAP curves (E). The orange circles in (D) indicate the bleached area during FRAP experiments, and the time after bleaching is indicated on top. Scale bars, 5 μm. (**F**) Nuclear GFP signal shows a strong increase in recovery half-life time upon OS. Data are from three experiments, and triangles indicate means of individual replicates ($n = $ cells 24 in control and $n = 22$ cells in OS).

of individual tomograms, the average NPC diameter correlated strongly with the average INM-ONM distance (Spearman correlation coefficient = 0.4803) (Fig. 7K).

Finally, we established that NPC constriction is reversible [prediction (v)]. Because OS conditions lead to a strong and homogeneous constriction of NPC diameters, we performed an OS recovery experiment. We analyzed 278 NPCs structurally by STA from

cells that were previously exposed to a OS and shifted back to glucose control medium. Measurements of individual NPC diameters confirmed NPC diameter reversibility (Fig. 6A). As expected, the INM-ONM distance and nuclear volume recovered concomitantly, whereas the nuclear membrane surface–to-NPC ratio remained constant (Fig. 7, E, J, and K, and fig. S18D). These findings further underscore a model in which increasing NE tension causes

NPC dilation, whereas a reduction of NE tension allows the NPC scaffold to relax and constrict (Fig. 8).

### Conclusions

Our study reveals that NPCs within living cells populate a much larger conformational space than previously anticipated. Massive conformational changes mediate NPC constriction and dilation in response to physiological cues,

## A



## B
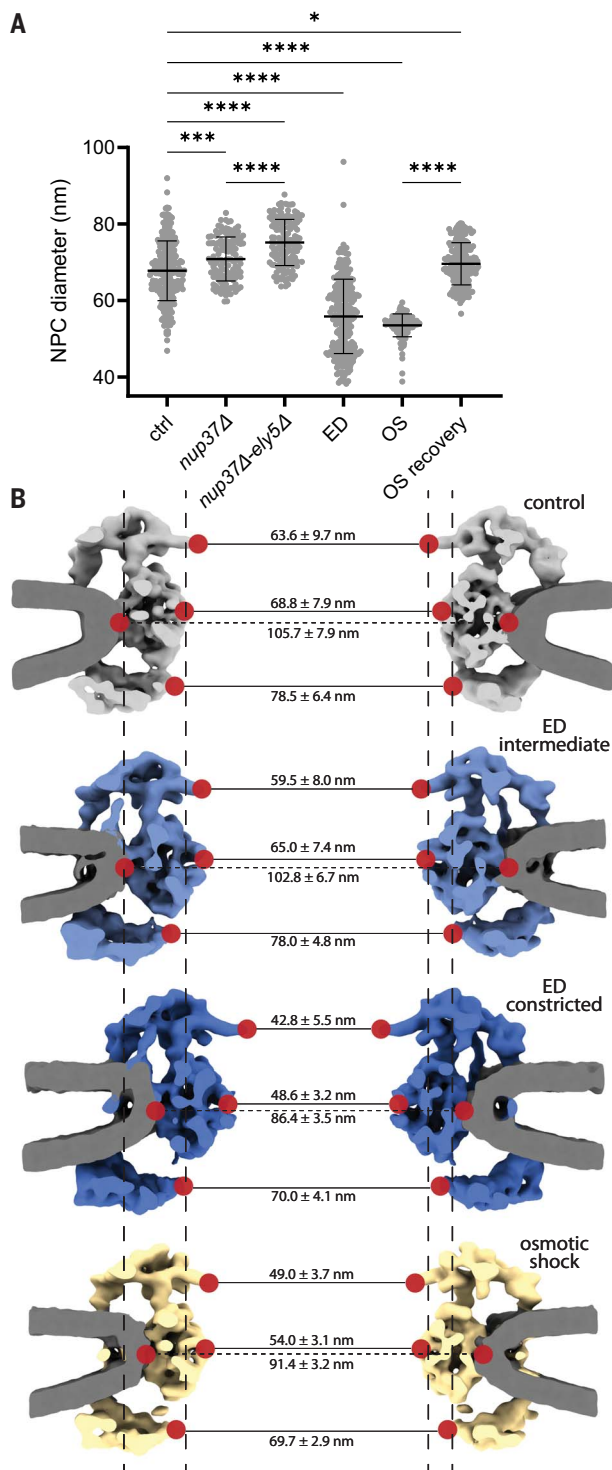


**Fig. 6. NPC diameter measurements across different conditions.** (**A**) Analysis of NPC central channel diameters measured at the equatorial center of the IR subcomplex based on subunit positions obtained by STA under control, *nup37Δ*, *nup37Δ-ely5Δ*, ED, OS, and OS recovery conditions. Data are from one or more experiments [means ± SDs; $n$ = 270 NPCs (control), $n$ = 129 NPCs (*nup37Δ*), $n$ = 141 NPCs (*nup37Δ-ely5Δ*), $n$ = 271 NPCs (ED), $n$ = 141 NPCs (OS), and $n$ = 197 NPCs (OS recovery)]. One-way analysis of variance (ANOVA) and Šidák's multiple comparison test; ****$P$ < 0.0001; ***$P$ < 0.001; *$P$ < 0.05 (see also fig. S17). (**B**) Same as Fig. 3 but shown as cutaway side view and overlaid with diameter measurements of individually aligned rings. Measurements are taken at the INM-ONM fusion points (dashed horizontal lines) and the most centrally exposed scaffold points (solid horizontal lines). Positions outlining the central channel were chosen corresponding to the tip of the mRNA export platform in the cytoplasmic side, the equatorial center of the IR subcomplex, and the tip of the inner nuclear Nup85 arm. The vertical lines represent the positions of the respective measurement points in the control conformation. Data are from one or more experiments (means ± SDs; $n$ = 270 NPCs in control, $n$ = 136 NPCs in intermediate ED, $n$ = 68 NPCs in most constricted ED, and $n$ = 141 NPCs in OS).

complex regions (movies S7 and S8). Those are, however, distinct from the previously proposed conformational sliding (*15*) and consistent with an overall preserved intrasubcomplex arrangement (*19, 20*).

It has been suggested that mechanical forces directly applied to the NE could regulate transport of mechanosensitive cargo and alter NPC diameters (*25, 60, 61*). Our data point to a model where NE tension regulates NPC diameter (Fig. 8). During OS and ED, NPC constriction is dependent on nuclear shrinkage and a reduction in INM-ONM distance, which both indicate a reduced NE tension (Fig. 7). Furthermore, the conformational changes of the NPC scaffold appear to be dictated by the movement of the nuclear membranes. During dilation and constriction, the IR spokes move strictly together with the fused INM and ONM. Finally, the knockout of the nonessential Y-complex members Nup37 and Ely5 leads to an increased flexibility and NPC dilation compared with control cells (Fig. 6A), suggesting that the NPC counteracts lateral forces imposed by NE tension, which keep it in an open conformation. Thus, the loss of NE tension leads to a relaxation and constriction in both ED and OS conditions.
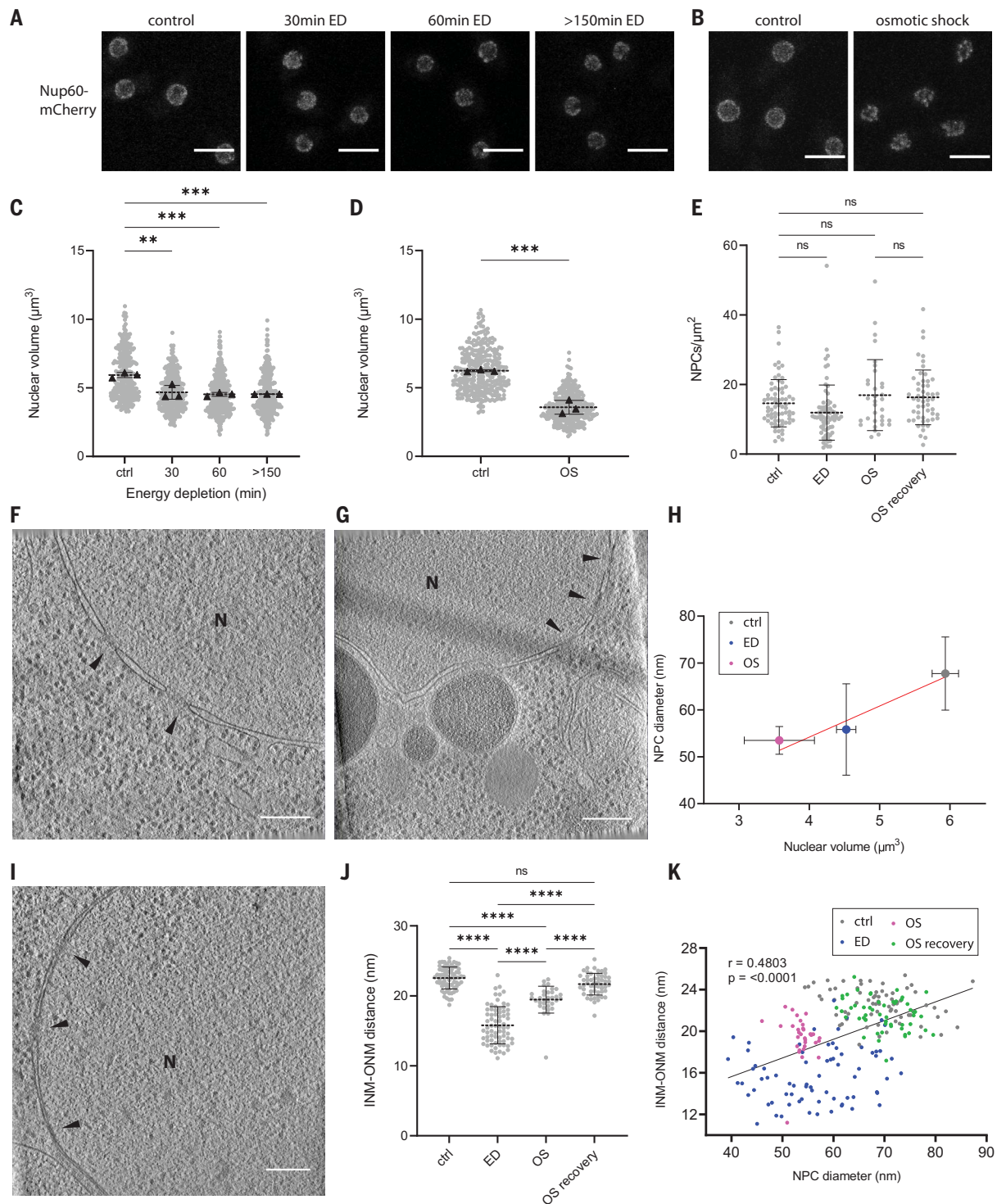
The unexpected split Y-complex arrangement of *S. pombe* breaks the long-standing dogma of a three-ringed architecture. This differential cytoplasmic and nuclear architecture, however, helps in assessing how the double–Y-complex arrangement contributes to the mechanical robustness of NPC architecture. The double–Y-complex ring arrangement of the NR constricts much less than the IR and the cytoplasmic structures. Knockouts of Y-complex components within the head-to-tail contact region destabilize the NR and lead to NPC dilation. These findings suggest that the Y-complex ring arrangement provides rigidity to the overall cylindrical architecture. It thus appears plausible that mechanical stress load on the NE—e.g., during cell migration or in osmotically variable environments that may result in unfavorable NE rupture events—imposed an evolutionary selection pressure for higher numbers of Y-complexes and ring formation in mammals or algae. By contrast, organisms less exposed to mechanical NE stresses, such as *S. cerevisiae* or *S. pombe*, reduced their Y-complex copy numbers and head-to-tail contacts during evolution. The NPC scaffold may have a wider range of functions beyond providing grafting sites for FG-Nups. It conformationally responds to mechanical cues and thus may have stabilizing but also mechanically sensory functions (*25, 60, 61*).

### Materials and methods
#### S. pombe culture and cryo-EM grid preparation

Frozen stocks of *S. pombe* cells were freshly thawed and maintained on YES-agar plates

such as the energy status of the cell or exposure to OS. Notably, ED resulted in a large heterogeneity of NPC constriction levels and two subpopulations with intermediate and strongly constricted NPC diameters. The average diameter observed under OS conditions was more defined at ~55 nm, with a relatively small standard deviation (Fig. 6A). This finding is consistent with the idea that

OS affects membrane tension more directly than ED.

The observed conformational changes involve stretching the Y-complexes but are particularly pronounced at the IR, where the spokes move alongside the fused INM and ONM. Notably, the spokes do not move entirely as rigid bodies, but some conformational changes occur within the Nup155 and Nsp1

**Fig. 7. NE tension is reduced during ED and OS and leads to NPC constriction.**
(**A**) Maximum projections of Nup60-mCherry channel from live-cell imaging confocal stacks of NLS-GFP-NLS and Nup60-mCherry–expressing cells used for nuclear shape and volume analysis. Scale bar, 5 μm. (**B**) Same as (A) but for cells expressing ubiquitous sfGFP and Nup60-mCherry under OS conditions. (**C** and **D**) Quantification of nuclear volume based on 3D reconstructions of Nup60-mCherry signal corresponding to (A) and (B). Data are from three experiments, and triangles indicate means of individual replicates (means ± SDs; $n$ = 300 nuclei per condition under ED and $n$ = 300 nuclei per condition under OS conditions). One-way ANOVA and Dunnett's multiple comparison test; ***$P$ < 0.001;

**$P$ < 0.01. (**E**) Number of NPCs per estimated NE surface area under control, ED, OS, and OS recovery conditions (see Materials and methods). Data are from one or more experiments (means ± SDs; $n$ = 71 tomograms under control, $n$ = 72 tomograms under ED, $n$ = 33 tomograms under OS, and $n$ = 53 tomograms under OS recovery conditions). One-way ANOVA and Šidák's multiple comparison test; ns indicates not significant, $P$ > 0.05. (**F** and **G**) Deconvolved slice through representative tomograms under control (F) and OS conditions (G). N marks the nucleus, and arrowheads mark NPCs. Scale bars, 200 nm. (**H**) Mean NPC diameter (see also Fig. 6A) plotted against mean nuclear volume [same as (C) and (D)] under and control and 60 min after ED and OS conditions. Linear regression

(red line) of mean nuclear volume values against scattered distribution of NPC diameters with means ± SDs and *n* values from (Fig. 6A) indicates a correlation between nuclear volume and NPC diameter. Data are from one or more experiments [coefficient of determination ($R^2$) = 0.3598]. (**I**) Deconvolved slice through representative tomograms under ED conditions. N marks the nucleus, and arrowheads mark NPCs. Scale bar, 200 nm. (**J**) Measurement of median INM-ONM distance per tomogram under control, ED, and OS conditions shows a clear decrease of INM-ONM distance during ED and a slight decrease during OS. Data are from one or more experiments (means ± SDs; *n* = 71 tomograms

under control, *n* = 72 tomograms under ED, *n* = 33 tomograms under OS, and *n* = 53 tomograms under OS recovery conditions). One-way ANOVA with Tukey's multiple comparison test; ****$P < 0.0001$; ns, $P > 0.05$. (**K**) The mean NPC diameter per tomogram plotted against the median INM-ONM distance per tomogram shows a strong positive correlation. Data are from one or more experiments (*n* = 71 tomograms under control, *n* = 72 tomograms under ED, *n* = 33 tomograms under OS, and *n* = 53 tomograms under OS recovery conditions). Spearman correlation coefficient (*r*) and *P* values are plotted, and the black line represents a simple linear regression line.

(YES-broth from Formedium +20 g agarose/L) at 30°C for maximum 3 days and re-streaked on fresh YES-plates before liquid culture inoculation. Five to 10 ml YES-broth were inoculated with individual colonies and incubated over night at 30°C shaking at 200 rpm, where $OD_{600}$ (the optical density of a sample measured at a wavelength of 600 nm) was kept below 1.0. Cryo-EM grid preparation was performed with a Leica EM GP plunger with a set chamber humidity of >90% and temperature of 30°C. A volume of 3.5 to 4 µl cell suspension with previously adjusted $OD_{600}$ to 0.3 were applied to Cu200 or Au200 mesh R2/1 $SiO_2$ grids (Quantifoil) glow discharged on each side for 45 s before sample application. The grids were blotted with Whatman 597 paper for 1 to 2 s and plunge-frozen in liquid ethane or a mix of ethane-propane (60 and 40%) at −189°C or −194°C, respectively. A list of all yeast strains and their source used in this study can be found in table S2.

### C. thermophilum *culture and cryo-EM grid preparation*

*C. thermophilum* (La Touche) *var. thermophilum* [from DSMZ, Braunschweig, Germany (no. 1495)] mycelium was maintained on CCM-plates, as described in (*62*). For cryo-EM grid preparation, Au200 mesh R2/1 $SiO_2$ grids (Quantifoil) were glow discharged on both sides for 45 s and placed on the CCM-plates at the edge of the mycelium growth rim with the $SiO_2$ foil facing up. Plates were incubated at 55°C until the mycelium covered at least half of the grid, typically 2 to ~3.5 hours. Grids were then mounted in the chamber of a Leica EM GP plunger with a set chamber humidity and temperature at >90% and 55°C, respectively. Before plunge freezing in liquid ethane at −186°C, 3.5 µl plunging phosphate buffer (5% trehalose, 0.013 M $Na_2HPO_4$, 0.045 M $KH_2PO_4$, pH 6.5) were applied to the sample and blotted for 2 s with Whatman 597 paper.

### Generation of knockout and fluorescently tagged S. pombe *strains*

A *nup37Δ* knockout cassette containing a clonNat resistance marker corresponding to pFA6a-natMX6 (*63*), flanked by 70-basepair-long homologous sequences to the nup37 gene was synthesized by Geneart and transformed

in a K972 h- wild-type (WT) *S. pombe* strain after a modified protocol from (*64*).

The *nup37Δ-ely5Δ* strain was generated by crossing the *nup37Δ* strain with an *ely5Δ* strain (*36*), provided by the Schwartz laboratory at MIT in Cambridge, Massachusetts, USA. Sporulation was triggered on sporulation plates prepared from SpoVB salts containing 8.2 g NaAc, 1.9 g KCl, 2.9 ml $MgSO_4$ 1 M, and 4.1 ml 5 M NaCl and 20 g agarose in 1 L $H_2O$. Tetrads of sporulated colonies were dissected in 40 µl sorbitol 1 M with 10 µl zymolyase-T100. Selected colonies were replica plated on selection plates containing 100 µg/ml clonNat (Jena Bioscience) or 100 µg/ml G418 (Sigma-Aldrich) and double gene knockout was confirmed by polymerase chain reaction (PCR).

To generate the strains CZ001 [expressing ubiquitous free super-folder GFP (sfGFP) with a Nup60-mCherry marker for FRAP analysis] and CZ007 (expressing NES-sfGFP-NES construct with a Nup60-mCherry marker), a Nup60-mCherry tagging cassette was amplified by PCR from isolated genomic DNA of the GD250 strain (*65*), provided by the Baum laboratory at MRC LMCB London, UK. The product was transformed into the sfGFP or the NES-sfGFP-NES expressing strain (AV0890 and AV1201, respectively) (*66*) obtained from the Yeast Genetic Resource Center (YGRC), as described above.

### ED of S. pombe *cells*

Overnight cultures of *S. pombe* cells were grown at 30°C in 5 ml dextrose-free Edinburgh minimal medium (EMM) supplemented with 20 mM glucose (glucose-control medium) while cell density was kept below $OD_{600}$ 0.8. Cells were collected and adjusted to obtain a cell amount of ~1 ml of cells with $OD_{600}$ ~0.3 by centrifugation in Eppendorf tubes at 4000 rpm for 3 min at room temperature. Cells were then washed three times with 1 ml of ED buffer [20 mM 2-deoxy-glucose (Sigma-Aldrich) in dextrose free EMM and 10 µM antimycin A (Sigma-Aldrich)] and resuspended in 1 ml of ED buffer. Control samples were washed three times in glucose control medium. For EM-grid preparation cells were incubated for 1 hour at 30°C on a table-top shaker at 900 rpm. The cell concentration was adjusted to an $OD_{600}$ of 0.2 before EM-grid preparation, as described above.

### ED recovery experiments and colony counting viability assays

For recovery experiments, cells were energy depleted as described above and shifted back to glucose control medium ~1 hour after ED. Light microscopy experiments were performed ~20 min after shift back to energy rich medium.

For colony counting, three biological replicates of WT cells were cultivated and energy depleted for 1 hour, as described above. The corresponding control samples were washed in glucose control medium. All samples were then washed and taken up in glucose control medium and 1000 cells were plated on fresh YES plates in duplicates. Colonies were counted after incubation at 30°C for 3 days, and values were reported as mean survivability corrected for plating efficiency in control conditions. For spot assays replicates were prepared as described above and the concentration of each sample was adjusted to $OD_{600}$ = 0.1. A serial dilution with 10x dilution steps was then spotted on a fresh YES plate.

### OS of S. pombe *cells*

OS experiments were performed with *S. pombe* cells expressing ubiquitous sfGFP and mCherry-tagged Nup60 (strain CZ001). Cells were grown at 30°C in 5 ml dextrose-free Edinburgh minimal medium (EMM) supplemented with 20 mM glucose (glucose-control medium) while cell density was kept below $OD_{600}$ 0.8. Cells for plunge freezing were grown to $OD_{600}$ of 0.6 and concentrated 2x in 1.5 ml Eppendorf tubes by centrifugation at 4000 rpm for 3 min before OS, whereas cells for light microscopy analysis were grown to $OD_{600}$ 0.4 before OS exposure. The OS was induced by diluting the cell suspension 1:1 with glucose control medium containing 2.4 M sorbitol, resulting in a OS exposure to 1.2 M sorbitol. Before plunge freezing cells were checked by fluorescent light microscopy to confirm the OS reaction and cryo-EM grids were subsequently prepared as described above 1 to 12 min after OS exposure. Light microscopy experiments were performed as described below. In OS recovery experiments cells were treated with 1.2 M sorbitol for ~10 min as described above and subsequently shifted back to glucose control medium where they were allowed to equilibrate for 30 to
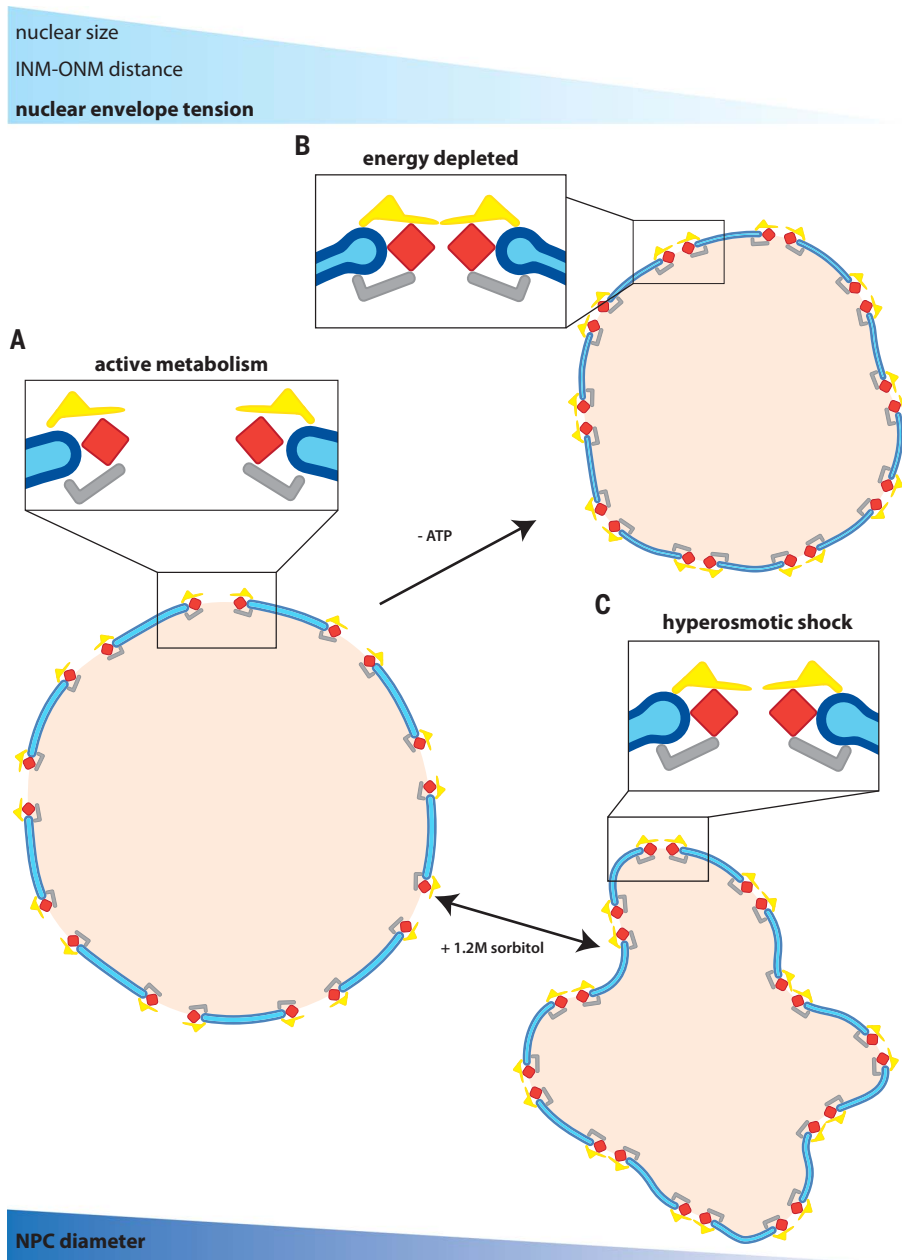
**Fig. 8. Conceptual model of how of NE tension regulates NPC diameter.** (**A**) NPCs adopt a dilated conformation in metabolically active cells. (**B** and **C**) Both ED (B) and OS (C) lead to a shrinkage of nuclear volume, a reduced INM-ONM distance, and an increased nuclear deformation, all of which point to a reduction in NE tension under both conditions. Such reduced NE tension leads to a constriction of the NPC scaffold architecture, where the central channel volume is reduced to approximately half compared with that in metabolically active cells.

40 min before cryo-EM grid preparation, as described above.

*Live-cell fluorescence microscopy and FRAP imaging*

Ibidi μ-Slide eight-well Ibidi-treat dishes were coated with 1 mg/ml Concanavalin A (Sigma-Aldrich) in phosphate-buffered saline (PBS) for 10 to 40 min at room temperature and washed three times with ddH$_2$O. Then, 300 μl of energy-depleted cells were seeded into the Ibidi μ-Slide dish and 150 μl of control cells were seeded and topped up with 150 μl glucose control medium to lower the amount of seeded cells and allow cells to keep dividing. Time of ED was measured from the first wash in ED buffer, typically ~12 min before finalizing the final wash and seeding eight-

well dishes. Live-cell imaging and FRAP experiments were all performed on a laser scanning confocal microscope Zeiss LSM-780 equipped with an incubation chamber maintained at 30°C. All images were acquired with a Plan-Apochromat 63x/1.40 Oil differential interference contrast (DIC) objective.

For live-cell imaging of GD250 and CZ007 1532x1532 pixel z-stacks were acquired with a pixel size of 0.0887 μm, an optical section of 0.8 μm, and z-step of 0.38 μm using sequential line scanning and two line averaging rounds with 0.426 μs pixel-dwell time. GFP was excited with a 488 nm line of argon laser and detected with GaAsP spectral detector in the range 500 to 550 nm. mCherry was excited with a DPSS laser at 561 nm and detected with GaAsP spectral detector in the range 568 to 620 nm. Per image stack, 15 to 17 z-slices were acquired to cover the entire *S. pombe* cells. In total, three independent biological replicates were acquired in three independent experiments with each containing about five individual z-stacks. For energy-depleted cells, z-stacks were acquired at time intervals of 30 to 50 min, 55 to 70 min, and 150 to 180 min after ED (after first wash with ED buffer), and control conditions were acquired more than 2 hours after sample preparation. For energy-depleted cells, data acquisition of each time point was started with the first z-stack the given time point after ED. Z-stacks of osmotically shocked CZ001 cells were acquired 1 to 16 min after hypertonic medium exposure.

FRAP measurements of bleached nuclear and cytoplasmic GFP signal in the CZ001 strains were performed to measure passive nuclear transport and cytoplasmic diffusion, respectively.

Passive nucleocytoplasmic transport was measured by individual FRAP experiments performed in the GFP channel consisting of a time series of 140 152x90 pixel (13.6 μm × 8.1 μm) frames acquired over 138.45 s with an interval of 1 s between different frames, a frame time of 0.17 s, and a pixel size of 0.09 μm. The 488 nm line of the argon laser was used both for bleaching and for excitation during time lapse imaging. Bleaching was performed after acquiring 10 images. One bleaching iteration of 1.2 s was performed in a circular area with a diameter of 33 pixel (2.97 μm), previously assigned manually based on the Nup60-mCherry NE outline to cover the nuclear area. Per individual biological replicate independent time series were acquired on individual cells over a period 30 to 210 min after ED, i.e., after the first wash with ED buffer. In total, 48 to 55 FRAP experiments per biological replicate were performed consecutively with an interval of ~3 to 5 min between the individual measurements. Control measurements were performed after completion of

data acquisition on energy-depleted cells i.e., >210 min after sample preparation.

To measure cytoplasmic diffusion, FRAP datasets were acquired in the GFP channel with image dimensions of 80x30 pixel (13.6 μm × 5.1 μm), a pixel size of 0.17 μm, and 140 frames over a period of 2.11 s with a time interval between frames equal to 0.03 s. A rectangular area covering around half of the *S. pombe* cytoplasm and excluding the nucleus was bleached after acquiring 20 initial images. One bleaching iteration was performed in 20 ms with 100% power of 488 laser line and additional 40% of 405 nm laser line. In three independent biological replicates each, eight individual FRAP experiments at time points 30 min (27 to 44 min), 60 min (55 to 68 min), and >150 min (155 to 168 min) after ED were recorded on individual cells. Control measurements were performed after 180 min of sample preparation. FRAP experiments of CZ001 cells exposed to a OS were performed as described above for ED with the following modifications: Each measurement was performed in three biological and eight subsequent technical replicates ranging over a timeframe of 3 to 25 min after OS exposure. To accommodate for the significantly slower cytoplasmic diffusion upon OS, the imaging parameters described above for nuclear FRAP were used where a 33x33 pixel square was bleached within the cytoplasm and recovery was measured over 120 s with a 1-s interval.

### Quantification of fluorescence microscopy images and FRAP analysis

To quantify the localization of NLS-GFP in GD250, z-stacks were maximum projected and the ratio of the average pixel intensity of a circular area within the nucleus compared with a similar area in the cytoplasm was measured manually in Fiji (*67*). The nuclear position was determined in the Nup60-mCherry channel. Cells that were not well attached to the eight-well dish and moving during z-stack acquisition or not entirely contained within the z-stack were removed before analysis, and cytoplasmic areas of clearly visible vacuoles were avoided. NES-GFP localization signal was quantified similarly as described above for NLS-GFP. To avoid signal bias from above and below the nucleus, only a single image slice approximately at the central plane of each cell was quantified.

Nuclear volume and sphericity of GD250 and CZ001 z-stacks were quantified based on 3D reconstructions of individual n of the Nup60-mCherry (with excluded areas of cells moving or not entirely contained within the imaged volume) using the 3DMembraneReconstruction (*68*) workflow in Mathwork's MATLAB.

FRAP curves were analyzed with FRAPAnalzer 2.1.0 (*69*). In brief, a double normalization was carried out normalizing against the back-

ground and the entire cellular surface as reference. Recovery half-life times were extracted by fitting a one exponential recovery equation to the normalized data. In the case of nuclear FRAP experiments under OS conditions, a two-exponential fitting was performed to account for the first (fast) recovery most likely corresponding to recovery of molecules bleached outside of the nucleus and a second (slower) recovery corresponding to the nuclear fluorescence recovery, the half-life time of the latter was reported as nuclear fluorescence half-life time. Moving cells and cells where the nuclear signal did not recover to a plateau were excluded from analysis.

### Cryo-FIB milling

Plunge-frozen sample grids were FIB milled in an Aquilos FIB-SEM (Thermo Fisher) as previously described (*4*). In brief, samples were sputter coated with inorganic platinum at 10 kV voltage and 10 mPa argon gas pressure for ~10 s (Pt-sputtering). Subsequently a protective layer of organometallic platinum was deposited using the gas injection system (GIS-coating) for ~12 s. If needed, a second round of Pt-sputtering was performed to avoid charging during FIB milling. Between 5 and 10 lamellae per grid were milled in a step-wise fashion and polished to a final thickness of <280 nm using decreasing FIB current steps of 1 nA, 0.5 nA, 0.3 nA, and 50 pA. Before unloading the sample, an additional layer of Pt was deposited for 1 s to avoid charging effects during subsequent imaging in the transmission electron microscope (TEM).

### Automated tomogram acquisition

The majority of WT *S. pombe* tomograms (136/178) as well as all tomograms from knockout strains were acquired on a Titan Krios G3 (Thermo Fisher), operating at 300 keV and equipped with a Gatan K2 Summit direct electron detector and energy-filter. All tilt-series (TS) were acquired in dose-fractionation mode at 4k × 4k resolution at a nominal pixel size of 3.45 Å. Automated TS acquisition was performed as described previously (*4*) using a dose-symmetric acquisition scheme (*70*) with an effective tilt range of −50° to 50°, considering a tilt-offset to compensate for the lamella angle (typically positive or negative 8° to 13°) (*4*), a 3° tilt increment, a total dose of 120 to 150 e/Å² , and target defocus of −1.5 to −4.5 μm.

The remaining 42 WT tomograms and 15 of the total 76 tomograms from energy-depleted *S. pombe* cells were acquired on a Titan Krios (Thermo Fisher) equipped with a Gatan K2 Summit direct electron detector and energy-filter and a Volta potential phase plate (VPP) (*71*). Automated dose-symmetric tilt series acquisition was performed in 4k × 4k dose-fractionation mode with a nominal pixel size

of 3.37 Å using a total dose of 100 to 125 e/Å² distributed over a tilt range of −60° to +60° or −50° to 50° with and a tilt step interval of 3° or 2°, respectively, a defocus range of −2 to −4 μm, and conditioning the VPP by exposure to the electron beam up to 5 min. An additional 11 tomograms of ED *S. pombe* cells were acquired using the same parameters but without usage of the VPP. All 57 tomograms of cells exposed to a OS were acquired with similar parameters including an effective tilt range of −50° to 50°, considering a tilt-offset to compensate for the lamella angle, a 3° tilt increment, a total dose of 120 to 150 e/Å², and target defocus of −2 to −5 μm.

The remaining 50 tomograms of ED *S. pombe* cells were acquired on a Titan Krios G3 (Thermo Fisher) operating at 300 keV equipped with a Gatan K3 direct electron detector and energy-filter operated in dose-fractionation mode and 5.7k × 4k resolution with a nominal pixel size of 3.425 Å. Automated dose-symmetric tilt series acquisition was performed with a nominal defocus range of −2 to −3.5 μm, an effective tilt range of −50° to 50° including a tilt offset to compensate for the lamella pretilt, a tilt step increment of 3°, and a total dose of 133 e/Å².

All 78 tomograms of cells recovered from a OS were acquired on a Titan Krios G2 (Thermo Fisher) equipped with a Gatan K3 direct electron detector and energy-filter with similar parameters as above including an effective tilt range of −50° to 50°, considering a tilt-offset to compensate for the lamella angle, a 3° tilt increment, a total dose of 142 e/Å², a target defocus of −2 to −5 μm, and a nominal pixel size of 3.372 Å. *C. thermophilum* tomograms were acquired as described above for WT *S. pombe* tomograms with a total dose of 130 to 140 e/Å² and a target defocus range of −2 to −4 μm.

### Image preprocessing and tomogram reconstruction

Images were preprocessed, and contrast transfer function (CTF) was estimated as described previously (*4*). Tilt series were aligned automatically in a tailored workflow using the IMOD package including the patch-tracking functionalities (*72*). In detail, four-times binned (pixel size: 1.348 nm) and dose-filtered TS were low-pass filtered with seven empirically predefined low-pass filter parameters and seven initial patch-tracking attempts using 7x7 patches per tilt were performed in IMOD. The filter-set and patch tracking output yielding the lowest alignment residuals during the initial round of patch-tracking was selected for further iterative refinement. At each iteration, the contour with the largest residual error was removed before the next round of patch-tracking. This process was repeated until the overall residual dropped below 0.5 pixel or until a ratio of known/unknown in the IMOD tilt

align program dropped below a threshold of 10. The final aligned TS were reconstructed using the SIRT-like filtering option in IMOD (*73*) and manually inspected. Only tomograms yielding a high-quality alignment, both, visually and in terms of overall residual error (typically better than 1 pixel) were used for 3D CTF correction using the phase-flipping option in novaCTF (*74*) and subsequent STA workflow.

### NE segmentation and tension analysis

Four-times binned 3D CTF-corrected tomograms were deconvolved in MATLAB using tom_deconv function (https://github.com/dtegunov/tom_deconv) and subsequently segmented using the convolutional neural network (CNN)–based tomogram segmentation workflow in EMAN2.2 (*75*) using a custom trained CNN to recognize NEs. The resulting segmentation was improved by applying the tensor voting–based membrane segmentation workflow TomoSegmemTV (*76*). The final binary segmented volume was manually inspected and curated, whereby false positive density such as NE connected ER was removed and tomograms resulting in overall inferior segmentation quality were excluded. Binary segmented NE volumes were subsequently loaded into MATLAB where a sphere was fitted to the coordinates of each individual segmentation. On the fitted sphere surface a sampling grid was defined with a kernel size (distance between sampling points) of 20 pixel (resulting in a subdivision of the spherical surface in ~27 nm × 27 nm patches). At each sampling point several measurements were performed.

First, at each sampling point the mean radius of all segmented voxels within a 20-pixel thick ray extending form the center of the fitted sphere through the sampling point were measured and the difference between the resulting mean NE radius and the fitted sphere radius was reported as deviation of the NE form a perfect sphere at each given sampling point. For each individual tomogram the variance or standard deviation of the deviation form a perfect sphere was then used as a measure of NE wobbliness (how much the NE deviates form a perfect sphere).

Second, the INM-ONM distance at each sampling point was measured by analyzing the distribution of radii of all voxels belonging to the NE segmentation within the 20-pixel-thick ray at each sampling point. Only radius distributions which showed a bimodal distribution were further used to perform a K-means clustering and obtain the mean NE radius of two classes. Sampling points which did not show a bimodal radius distribution were omitted. The shorter radius was then attributed to the INM radius, whereas larger value described the ONM radius at the given sampling point. The difference between the INM and ONM radius was reported as INM-ONM distance at any given sampling point, and the median over the entire tomogram was used as INM-ONM distance measurement for each individual tomogram.

Third, the total segmented NE surface was estimated by projecting the segmented NE voxels on the fitted sphere surface. Subsequently all sampling points covering at least one NE voxel within the 20-pixel radius were counted as 729 nm$^2$ (27 nm × 27 nm) membrane patch each and summed up to yield the total estimated NE surface. The number of initially picked NPCs (see below) per tomogram was divided by the corresponding estimated NE surface area to estimate the number of NPCs per square micrometer of NE.

### Particle identification and STA

NPC coordinates and initial orientations were determined manually in four-times binned SIRT-like filtered (*73*) tomograms as described earlier (*4*). Additionally, a model describing the lamella slab geometry was generated manually by picking the coordinates of all eight corners of the lamella slab for each tomogram. Particle extraction, subtomogram alignment, and averaging (STA) was performed with novaSTA (*77*) from 3D CTF-corrected tomograms, as described previously (*4*). Initial alignment of NPCs was carried out using eight- and four-times binned particles. After obtaining an initial four-times binned average, coordinates of the eight individual NPC spokes were identified for symmetry-independent alignment, as described before (*6*). In brief, the coordinates of an individual subunit within the eightfold average was defined manually, and the remaining asymmetric subunit positions were calculated based on the eightfold symmetry (fig. S2A). The coordinates were then used to extract each individual asymmetric subunit form the original tomograms, where only subunits with coordinates retained in the lamella slab geometry model were retained to avoid the inclusion of subunits lying outside the FIB-milled lamellae. The individually extracted asymmetric subunits were then used for further alignment using a mask covering the entire asymmetric unit (cytoplasmic side, IR, and NR) (fig. S2B). After an initial subunit alignment, each subtomogram and its assigned orientation was inspected manually and misaligned or remaining false positive particles, i.e., subunits extracted outside of the FIB-milled lamellae, were removed. Subtomogram alignment was further continued using four- and two-times binned subtomograms, where the alignment was focused on the CR, IR, or NR using localized masks (fig. S2C). VPP data were excluded from further STA of the WT averages at the transition from bin4 to bin2 processing. If needed, the particle boxes were recentered around the individual rings to achieve better subtomogram alignment. In case of the WT subtomogram average, particles with low final cross correlation scores were removed for the final average. All subtomogram averages of WT, OS, and knockout datasets were b-factor sharpened empirically (*11*) and filtered to the given resolution determined on gold-standard FSC calculations at the 0.143 criterion. For ED averages, instead of b-factor sharpening, the amplitude of the final averages (containing VPP and defocus data) were matched to the amplitudes of a corresponding average generated by averaging only the defocus type subset of data (excluding all VPP data) with the EMAN2 (*78*) e2proc3d.py -matchto function, to overcome a previously described low-pass filter-like artifact occurring during STA of VPP data (*79*).

To generate the eightfold symmetric assemblies, the final individual ring maps were first fit to the initially aligned whole asymmetric unit map to find their correct relative position. The root mean square density value of all individual maps were scaled to similar values to allow appropriate representation of all three rings at a common threshold level. The resulting asymmetric unit was then assembled to an eightfold symmetric assembly based on the coordinates defined during the initial subunit extraction (see above).

Details about tomogram and particle numbers of each average can be found in table S3.

### Difference map calculation

To calculate the difference map of the *nup37Δ* and *nup37Δ-ely5Δ* knockout to the WT, the maps of the individual knockout rings were filtered according to their reported resolution (*nup37Δ* cytoplasmic side: 27 Å, IR: 27 Å, and NR: 31 Å; cytoplasmic side: 35 Å, IR: 35 Å, and NR: 34 Å of *nup37Δ-ely5Δ*, respectively) (table S3 and figs. S8 and S9), and WT maps were filtered to the corresponding knockout resolution. To account for different b-factors and amplitudes, the power spectra of the WT maps were adjusted to the corresponding knockout map using RELION (*80*) relion_image_handler -adjust_power command. To obtain comparable difference maps across the density of the individual knockout rings, the WT cytoplasmic and nuclear map were scaled to match the root mean square of the corresponding WT IR map. The WT and corresponding knockout maps were then brought to the same reference frame by fitting the maps against each other and difference maps of the individual rings were calculated in UCSF Chimera (*81*). The final maps are shown at the same threshold and overlaid with the difference map (WT minus knockout) and the inverse (negative threshold) of the difference map, respectively (Fig. 2 and figs. S8 and S9)

### NPC diameter and volume measurements

NPC diameters were measured with an in-house MATLAB script based on the final co-ordinates and orientations obtained for each individual subunit during STA. First a feature of interest in the subunit average was identified in UCSF Chimera (*81*) by placing a 1-voxel sphere mask on the point of interest. The offset between the center of the average and the mask was then used to calculate the co-ordinates of the area of interest within each averaged subunit in respect to the original tomograms. To calculate the diameter of each individual NPC, only NPCs with a subunit-occupancy of five or more were considered. For each individual NPC, vectors were derived connecting the opposing subunits. Based on those vectors, the center of each NPC was defined as the center of the intersection area between all vectors corresponding to a given NPC. The average distance between the newly identified center and each respective SU was chosen as a representative NPC radius for the given pore. By this means, an accurate average NPC radius measurement for a specific feature of interest within each individual NPC is obtained. Additionally, the z-translation of each subunit from the NPC center plane and the pairwise distance opposing subunits based on coordinates obtained from whole asymmetric subunit alignment were reported (fig. S17, A to G).

### Homology modeling

Modeling templates were detected and selected using HHpred server (*82*). Sequence alignments for modeling were refined in Swiss PDB Viewer (*83*). The models were built based on the templates and alignments using Modeller (*84*). The templates used for modeling are listed in table S4.

### Systematic fitting of SpNPC rigid bodies to cryo-ET maps

To assign the number of Y-complexes and IR subcomplexes, and to prepare the input for integrative modeling (fig. S5A), an unbiased global fitting approach was applied using several SpNPC structural models. Two of them were experimental x-ray structures previously published (*35*, *36*), whereas the remaining were homology modeled on the basis of *S. cerevisiae* and *C. thermophilum* NPC components (*20*, *85*–*88*) (table S4). All the aforementioned high-resolution structures were filtered to 40 Å before fitting. The resulting simulated model maps were subsequently fitted into individual segments of the SpNPC cryo-EM maps from this study by global fitting as implemented in UCSF Chimera (*81*). More precisely, structures of the Y-complex were fitted into cytoplasmic and NR segments of the cryo-EM SpNPC maps while the IR model was fitted in the IR. The segmented maps that

were used for fitting did not include NE density to eliminate the possibility of fits substantially overlapping with the membrane.

All fitting runs were performed using 100,000 random initial placements with the requirement of at least 30% of the simulated model map to be covered by the SpNPC density envelope defined at a low threshold. For each fitted model, this procedure resulted in ~250 to 17,200 fits with nonredundant conformations upon clustering. The cross-correlation about the mean (cam score, equivalent to Pearson correlation) score from UCSF Chimera (*81*) was used as a fitting metric for each atomic structure, similarly to our previously published works (*4*, *11*, *12*, *31*). The statistical significance of every fitted model was evaluated as a *P* value derived from the cam scores. The calculation of *P* values was performed by first transforming the cross-correlation scores to z-scores (Fisher's z-transform) and centering, from which subsequently two-sided *P* values were computed using standard deviation derived from an empirical null distribution [based on all obtained nonredundant fits and fitted using fdrtool (*89*) R-package]. Finally, the *P* values were corrected for multiple testing with Benjamini-Hochberg (*90*). Figures were produced by UCSF Chimera (*81*) and UCSF ChimeraX (*91*).

### Integrative modeling

Structural models of the SpNPCs were built using the integrative procedure (fig. S5) implemented in our Assembline software (*92*). Assembline implements a custom modeling pipeline based on Integrative Modeling Platform (IMP) (*93*) version 2.14 and Python Modeling Interface (PMI) (*94*). The pipeline is similar to the one we used previously for human and *S. cerevisiae* NPCs (*4*, *12*). The modeling procedure consisted of three steps (fig. S5B).

### Step 1

First, ensembles of alternative models of the individual rings in the control NPC were constructed. To model the cytoplasmic Y-complexes and NR, the input homology models were divided into smaller rigid bodies (with cut points corresponding to boundaries of published crystal structures) and simultaneously fitted to the cryo-ET map using the global optimization step in Assembline. In this step, first, libraries of alternative nonredundant fits for each rigid body were generated using the systematic fitting procedure described above. Then, the rigid bodies were fitted simultaneously to the maps of individual rings by sampling alternative fits from these libraries using the simulated annealing Monte Carlo method. To cover a large landscape of possible models, the optimization was repeated 4000 and 40,000 times for the cytoplasmic side and NR, respectively, with each repetition leading

to a candidate model. To achieve convergence and sampling exhaustiveness [assessed using the procedure by Viswanath *et al.* (*95*)], each repeat run was composed of 130,000 (cytoplasmic side) and 271,000 (NR) Monte Carlo steps at decreasing temperatures. The higher number of steps and models for NR was used because of the higher number of rigid bodies in this ring. The scoring function for the modeling optimization was a linear combination of the EM fit restraint represented as the *P* values of the precalculated rigid-body fits (from systematic fitting as described above), clash score (SoftSpherePairScore of IMP), connectivity distance between domains neighboring in sequence, a term preventing overlap of the protein mass with the NE, a restraint promoting the membrane-binding loops of Nup131, Nup132, and Nup120 to interact with the envelope, implemented using MapDistanceTransform of IMP [predicted by similarity to known or predicted ALPS motifs in human and *S. cerevisiae* homologs (*1*, *96*)], the restraint for Ely5 localization in the region identified based on the difference between the *nup37Δ* and *nup37Δ-ely5Δ* knockout NPC maps to the control NPC, and restraint for biochemically characterized interaction restraint between Ely5 and Nup120 (*36*). For the NR, a restraint promoting Nup37 localization from the difference between the *nup37Δ* NPC and the control NPC was also used. During the optimization, the structures were simultaneously represented at two resolutions: in Cα-only representation and in a coarse-grained representation, in which each 10-residue stretch was converted to a bead. The 10-residue bead representation was used for all restraints to increase computational efficiency except for the domain connectivity restraints, for which the Cα-only representation was used. Because the *P* values used for the EM restraint were derived from the original EM fit libraries generated with UCSF Chimera, the EM restraint can be regarded as an EM restraint derived from the full atom representation.

Owing to high structural conservation of the IR as determined by the systematic fitting, this ring was modeled by fitting a homology model of the entire IR built based on *S. cerevisiae* NPC, followed by the refinement with 50,000 Monte Carlo steps at a single temperature. The refinement involved the Monte Carlo simulated annealing optimization of the rigid bodies' rotations and translations, but this time without using the libraries of alternative non-redundant fits, allowing the rigid bodies to move in the EM map with small rotation and translation increments. The scoring function consisted of cross-correlation to the EM map (FitRestraint of IMP), domain connectivity restraint, the clash score, the envelope exclusion restraints as above, and a restraint for the membrane-binding loop of Nup155 (*12*).

## Step 2

The above steps led to ensembles of separate models for the cytoplasmic side, NR, and IR. To build the model of the full NPC, the alternative fits of each subunit in the cytoplasmic side and NR models were extracted into a new set of fit libraries. Then, together with the top-scoring model of the IR, the global optimization step was repeated using the new fit libraries and now fitting all subunits from all three rings of the NPC simultaneously. The resulting models were refined as above for the IR, leading to an ensemble of models of the full NPC. An elastic network restraint was used to keep the Ely5-Nup120 orientation similar in all rings.

## Step 3

To generate the models of the ED NPCs, the 1000 top-scoring models of the NPC under control conditions were fitted into the ED EM maps and optimized using the refinement procedure. The scoring function comprised the same restraints as for the refinement of the individual rings except for the restraint for Nup37 localization in the difference density. Each of the 1000 starting models was refined with 150,000 steps at five temperature levels leading to an ensemble of 1000 alternative models.

## Model analysis

To assess convergence and exhaustiveness of sampling, and to assess the precision of sampling and of the models, we used the procedure by Viswanath *et al.* (*95*). The quantities were assessed at each modeling step of the procedure (fig. S5B). The sampling precision for the control, ED medium, and constricted diameter were 8.4, 12.6, and 12.8 Å, respectively. At this sampling precision, we obtained two to four clusters of models with the model precision between 7.2 and 9.7 Å (fig. S5B). The clusters differed mostly in the orientations of Ely5, Nup120, and the N-terminal propeller of Nup133. The model with the orientation of Ely5 consistent with the model of the human NPC (*11*) was used as a representative model for the figures. For clarity, a single model was shown in the figures and the top 10 models for each ensemble were shown in fig. S5.

### REFERENCES AND NOTES

1. D. H. Lin, A. Hoelz, The Structure of the Nuclear Pore Complex (An Update). *Annu. Rev. Biochem.* **88**, 725–783 (2019). doi: 10.1146/annurev-biochem-062917-011901; pmid: 30883195

2. M. Beck, S. Mosalaganti, J. Kosinski, From the resolution revolution to evolution: Structural insights into the evolutionary relationships between vesicle coats and the nuclear pore. *Curr. Opin. Struct. Biol.* **52**, 32–40 (2018). doi: 10.1016/j.sbi.2018.07.012; pmid: 30103204

3. J. Mahamid *et al.*, Visualizing the molecular sociology at the HeLa cell nuclear periphery. *Science* **351**, 969–972 (2016). doi: 10.1126/science.aad8857; pmid: 26917770

4. M. Allegretti *et al.*, In-cell architecture of the nuclear pore and snapshots of its turnover. *Nature* **586**, 796–800 (2020). doi: 10.1038/s41586-020-2670-5; pmid: 32879490

5. G. J. Stanley, A. Fassati, B. W. Hoogenboom, Atomic force microscopy reveals structural variability amongst nuclear pore complexes. *Life Sci. Alliance* **1**, e201800142 (2018). doi: 10.26508/lsa.201800142; pmid: 30456374

6. M. Beck, V. Lučić, F. Förster, W. Baumeister, O. Medalia, Snapshots of nuclear pore complexes in action captured by cryo-electron tomography. *Nature* **449**, 611–615 (2007). doi: 10.1038/nature06170; pmid: 17851530

7. J. Sellés *et al.*, Nuclear pore complex plasticity during developmental process as revealed by super-resolution microscopy. *Sci. Rep.* **7**, 14732 (2017). doi: 10.1038/s41598-017-15433-2; pmid: 29116248

8. A. P. Schuller *et al.*, The cellular environment shapes the nuclear pore complex architecture. *Nature* **598**, 667–671 (2021). doi: 10.1038/s41586-021-03985-3; pmid: 34646014

9. V. Zila *et al.*, Cone-shaped HIV-1 capsids are transported through intact nuclear pores. *Cell* **184**, 1032–1046.e18 (2021). doi: 10.1016/j.cell.2021.01.025; pmid: 33571428

10. K. H. Bui *et al.*, Integrated structural analysis of the human nuclear pore complex scaffold. *Cell* **155**, 1233–1243 (2013). doi: 10.1016/j.cell.2013.10.055; pmid: 24315095

11. A. von Appen *et al.*, *In situ* structural analysis of the human nuclear pore complex. *Nature* **526**, 140–143 (2015). doi: 10.1038/nature15381; pmid: 26416747

12. J. Kosinski *et al.*, Molecular architecture of the inner ring scaffold of the human nuclear pore complex. *Science* **352**, 363–365 (2016). doi: 10.1126/science.aaf0643; pmid: 27081072

13. S. Otsuka *et al.*, Postmitotic nuclear pore assembly proceeds by radial dilation of small membrane openings. *Nat. Struct. Mol. Biol.* **25**, 21–28 (2018). doi: 10.1038/s41594-017-0001-9; pmid: 29323269

14. S. Otsuka *et al.*, Nuclear pore assembly proceeds by an inside-out extrusion of the nuclear envelope. *eLife* **5**, e19071 (2016). doi: 10.7554/eLife.19071; pmid: 27630123

15. J. Koh, G. Blobel, Allosteric regulation in gating the central channel of the nuclear pore complex. *Cell* **161**, 1361–1373 (2015). doi: 10.1016/j.cell.2015.05.013; pmid: 26046439

16. A. C. Meinema *et al.*, Long unfolded linkers facilitate membrane protein import through the nuclear pore complex. *Science* **333**, 90–93 (2011). doi: 10.1126/science.1205741; pmid: 21659568

17. R. Ungricht, M. Klann, P. Horvath, U. Kutay, Diffusion and retention are major determinants of protein targeting to the inner nuclear membrane. *J. Cell Biol.* **209**, 687–703 (2015). doi: 10.1083/jcb.201409127; pmid: 26056139

18. A. Boni *et al.*, Live imaging and modeling of inner nuclear membrane targeting reveals its molecular requirements in mammalian cells. *J. Cell Biol.* **209**, 705–720 (2015). doi: 10.1083/jcb.201409133; pmid: 26056140

19. H. Chug, S. Trakhanov, B. B. Hülsmann, T. Pleiner, D. Görlich, Crystal structure of the metazoan Nup62•Nup58•Nup54 nucleoporin complex. *Science* **350**, 106–110 (2015). doi: 10.1126/science.aac7420; pmid: 26292704

20. T. Stuwe *et al.*, Architecture of the fungal nuclear pore inner ring complex. *Science* **350**, 56–64 (2015). doi: 10.1126/science.aac9176; pmid: 26316600

21. V. Shahin, T. Danker, K. Enss, R. Ossig, H. Oberleithner, Evidence for Ca$^{2+}$- and ATP-sensitive peripheral channels in nuclear pore complexes. *FASEB J.* **15**, 1895–1901 (2001). doi: 10.1096/fj.00-0838com; pmid: 11532969

22. D. Stoffler, K. N. Goldie, B. Feja, U. Aebi, Calcium-mediated structural changes of native nuclear pore complexes monitored by time-lapse atomic force microscopy. *J. Mol. Biol.* **287**, 741–752 (1999). doi: 10.1006/jmbi.1999.2637; pmid: 10191142

23. A. Rakowska, T. Danker, S. W. Schneider, H. Oberleithner, ATP-Induced shape change of nuclear pores visualized with the atomic force microscope. *J. Membr. Biol.* **163**, 129–136 (1998). doi: 10.1007/s002329900377; pmid: 9592077

24. L. Kastrup, H. Oberleithner, Y. Ludwig, C. Schafer, V. Shahin, Nuclear envelope barrier leak induced by dexamethasone. *J. Cell. Physiol.* **206**, 428–434 (2006). doi: 10.1002/jcp.20479; pmid: 16110478

25. I. Liashkovich, A. Meyring, A. Kramer, V. Shahin, Exceptional structural and mechanical flexibility of the nuclear pore complex. *J. Cell. Physiol.* **226**, 675–682 (2011). doi: 10.1002/jcp.22382; pmid: 20717933

26. R. D. Jäggi *et al.*, Modulation of nuclear pore topology by transport modifiers. *Biophys. J.* **84**, 665–670 (2003). doi: 10.1016/S0006-3495(03)74886-3; pmid: 12524319

27. M. Eibauer *et al.*, Structure and gating of the nuclear pore complex. *Nat. Commun.* **6**, 7532 (2015). doi: 10.1038/ncomms8532; pmid: 26112706

28. Y. Zhang *et al.*, Molecular architecture of the luminal ring of the *Xenopus laevis* nuclear pore complex. *Cell Res.* **30**, 532–540 (2020). doi: 10.1038/s41422-020-0320-y; pmid: 32367042

29. G. Huang *et al.*, Structure of the cytoplasmic ring of the *Xenopus laevis* nuclear pore complex by cryo-electron microscopy single particle analysis. *Cell Res.* **30**, 520–531 (2020). doi: 10.1038/s41422-020-0319-4; pmid: 32376910

30. M. C. Field, M. P. Rout, Pore timing: The evolutionary origins of the nucleus and nuclear pore complex. *F1000Research* **8**, 369 (2019). doi: 10.12688/f1000research.16402.1; pmid: 31001417

31. S. Mosalaganti *et al.*, In situ architecture of the algal nuclear pore complex. *Nat. Commun.* **9**, 2361 (2018). doi: 10.1038/s41467-018-04739-y; pmid: 29915221

32. H. Asakawa *et al.*, Asymmetrical localization of Nup107-160 subcomplex components within the nuclear pore complex in fission yeast. *PLOS Genet.* **15**, e1008061 (2019). doi: 10.1371/journal.pgen.1008061; pmid: 31170156

33. J. Fernandez-Martinez *et al.*, Structure and Function of the Nuclear Pore Complex Cytoplasmic mRNA Export Platform. *Cell* **167**, 1215–1228.e25 (2016). doi: 10.1016/j.cell.2016.10.028; pmid: 27839866

34. P. Stelter *et al.*, Molecular basis for the functional interaction of dynein light chain with the nuclear-pore complex. *Nat. Cell Biol.* **9**, 788–796 (2007). doi: 10.1038/ncb1604; pmid: 17546040

35. X. Liu, J. M. Mitchell, R. W. Wozniak, G. Blobel, J. Fan, Structural evolution of the membrane-coating module of the nuclear pore complex. *Proc. Natl. Acad. Sci. U.S.A.* **109**, 16498–16503 (2012). doi: 10.1073/pnas.1214557109; pmid: 23019579

36. S. Bilokapic, T. U. Schwartz, Molecular basis for Nup37 and ELY5/ELYS recruitment to the nuclear pore complex. *Proc. Natl. Acad. Sci. U.S.A.* **109**, 15241–15246 (2012). doi: 10.1073/pnas.1205511109; pmid: 22955883

37. B. A. Rasala, A. V. Orjalo, Z. Shen, S. Briggs, D. J. Forbes, ELYS is a dual nucleoporin/kinetochore protein required for nuclear pore assembly and proper cell division. *Proc. Natl. Acad. Sci. U.S.A.* **103**, 17801–17806 (2006). doi: 10.1073/pnas.0608484103; pmid: 17098863

38. S. W. Baï *et al.*, The fission yeast Nup107-120 complex functionally interacts with the small GTPase Ran/Spi1 and is required for mRNA export, nuclear pore distribution, and proper cell division. *Mol. Cell. Biol.* **24**, 6379–6392 (2004). doi: 10.1128/MCB.24.14.6379-6392.2004; pmid: 15226438

39. K. Kelley, K. E. Knockenhauer, G. Kabachinski, T. U. Schwartz, Atomic structure of the Y complex of the nuclear pore. *Nat. Struct. Mol. Biol.* **22**, 425–431 (2015). doi: 10.1038/nsmb.2998; pmid: 25822992

40. S. J. Kim *et al.*, Integrative structure and functional anatomy of a nuclear pore complex. *Nature* **555**, 475–482 (2018). doi: 10.1038/nature26003; pmid: 29539637

41. T. Maimon, N. Elad, I. Dahan, O. Medalia, The human nuclear pore complex as revealed by cryo-electron tomography. *Structure* **20**, 998–1006 (2012). doi: 10.1016/j.str.2012.03.025; pmid: 22632834

42. M. C. Munder *et al.*, A pH-driven transition of the cytoplasm from a fluid- to a solid-like state promotes entry into dormancy. *eLife* **5**, e09347 (2016). doi: 10.7554/eLife.09347; pmid: 27003292

43. W. D. Richardson, A. D. Mills, S. M. Dilworth, R. A. Laskey, C. Dingwall, Nuclear protein migration involves two steps: Rapid binding at the nuclear envelope followed by slower translocation through nuclear pores. *Cell* **52**, 655–664 (1988). doi: 10.1016/0092-8674(88)90403-5; pmid: 3125984

44. N. Shulga *et al.*, In vivo nuclear transport kinetics in *Saccharomyces cerevisiae*: A role for heat shock protein 70 during targeting and translocation. *J. Cell Biol.* **135**, 329–339 (1996). doi: 10.1083/jcb.135.2.329; pmid: 8896592

45. W. A. Whalen, J. H. Yoon, R. Shen, R. Dhar, Regulation of mRNA export by nutritional status in fission yeast. *Genetics* **152**, 827–838 (1999). doi: 10.1093/genetics/152.3.827; pmid: 10388805

46. E. D. Schwoebel, T. H. Ho, M. S. Moore, The mechanism of inhibition of Ran-dependent nuclear transport by cellular ATP depletion. *J. Cell Biol.* **157**, 963–974 (2002). doi: 10.1083/jcb.200111077; pmid: 12058015

47. R. W. Wozniak, G. Blobel, M. P. Rout, POM152 is an integral protein of the pore membrane domain of the yeast nuclear envelope. *J. Cell Biol.* **125**, 31–42 (1994). doi: 10.1083/jcb.125.1.31; pmid: 8138573

48. P. Upla *et al.*, Molecular Architecture of the Major Membrane Ring Component of the Nuclear Pore Complex. *Structure* **25**, 434–445 (2017). doi: 10.1016/j.str.2017.01.006; pmid: 28162953

49. S. Abuhattum et al., Intracellular Mass Density Increase Is Accompanying but Not Sufficient for Stiffening and Growth Arrest of Yeast Cells. Front. Phys. 6, 131 (2018). doi: 10.3389/fphy.2018.00131

50. A. Miermont et al., Severe osmotic compression triggers a slowdown of intracellular signaling, which can be explained by molecular crowding. Proc. Natl. Acad. Sci. U.S.A. 110, 5725–5730 (2013). doi: 10.1073/pnas.1215367110; pmid: 23493557

51. R. P. Joyner et al., A glucose-starvation response regulates the diffusion of macromolecules. eLife 5, e09376 (2016). doi: 10.7554/eLife.09376; pmid: 27003290

52. G. Marini, E. Nüske, W. Leng, S. Alberti, G. Pigino, Reorganization of budding yeast cytoplasm upon energy depletion. Mol. Biol. Cell 31, 1232–1245 (2020). doi: 10.1091/mbc.E20-02-0125; pmid: 32293990

53. M. B. Heimlicher et al., Reversible solidification of fission yeast cytoplasm after prolonged nutrient starvation. J. Cell Sci. 132, jcs.231688 (2019). doi: 10.1242/jcs.231688; pmid: 31558680

54. A. J. Lomakin et al., The nucleus acts as a ruler tailoring cell responses to spatial constraints. Science 370, eaba2894 (2020). doi: 10.1126/science.aba2894; pmid: 33060332

55. V. Venturini et al., The nucleus measures shape changes for cellular proprioception to control dynamic cell behavior. Science 370, eaba2644 (2020). doi: 10.1126/science.aba2644; pmid: 33060331

56. A. Agrawal, T. P. Lele, Mechanics of nuclear membranes. J. Cell Sci. 132, jcs229245 (2019). doi: 10.1242/jcs.229245; pmid: 31308244

57. P. T. Tran, L. Marsh, V. Doye, S. Inoué, F. Chang, A mechanism for nuclear positioning in fission yeast based on microtubule pushing. J. Cell Biol. 153, 397–412 (2001). doi: 10.1083/jcb.153.2.397; pmid: 11309419

58. S. M. Schreiner, P. K. Koo, Y. Zhao, S. G. J. Mochrie, M. C. King, The tethering of chromatin to the nuclear envelope supports nuclear mechanics. Nat. Commun. 6, 7159 (2015). doi: 10.1038/ncomms8159; pmid: 26074052

59. A. Agrawal, T. P. Lele, Geometry of the nuclear envelope determines its flexural stiffness. Mol. Biol. Cell 31, 1815–1821 (2020). doi: 10.1091/mbc.E20-02-0163; pmid: 32583742

60. A. Elosegui-Artola et al., Force Triggers YAP Nuclear Entry by Regulating Transport across Nuclear Pores. Cell 171, 1397–1410.e14 (2017). doi: 10.1016/j.cell.2017.10.008; pmid: 29107331

61. B. Enyedi, P. Niethammer, Nuclear membrane stretch and its role in mechanotransduction. Nucleus 8, 156–161 (2017). doi: 10.1080/19491034.2016.1263411; pmid: 28112995

62. N. Kellner et al., Developing genetic tools to exploit Chaetomium thermophilum for biochemical analyses of eukaryotic macromolecular assemblies. Sci. Rep. 6, 20937 (2016). doi: 10.1038/srep20937; pmid: 26864114

63. H. Amelina et al., Sequential and counter-selectable cassettes for fission yeast. BMC Biotechnol. 16, 76 (2016). doi: 10.1186/s12896-016-0307-4

64. J. Bähler et al., Heterologous modules for efficient and versatile PCR-based gene targeting in Schizosaccharomyces pombe. Yeast 14, 943–951 (1998). doi: 10.1002/(SICI)1097-0061(199807)14:10<943::AID-YEA292>3.0.CO;2-Y; pmid: 9717240

65. G. Dey et al., Closed mitosis requires local disassembly of the nuclear envelope. Nature 585, 119–123 (2020). doi: 10.1038/s41586-020-2648-3

66. A. Vještica et al., A toolbox of stable integration vectors in the fission yeast Schizosaccharomyces pombe. J. Cell Sci. 133, jcs240754 (2020). doi: 10.1242/jcs.240754; pmid: 31801797

67. J. Schindelin et al., Fiji: An open-source platform for biological-image analysis. Nat. Methods 9, 676–682 (2012). doi: 10.1038/nmeth.2019; pmid: 22743772

68. J. F. Williams, S. G. J. Mochrie, M. C. King, A versatile image analysis platform for three-dimensional nuclear reconstruction. Methods 157, 15–27 (2019). doi: 10.1016/j.ymeth.2018.10.009; pmid: 30359725

69. A. Halavatyi, S. Terjung, in Standard and Super-Resolution Bioimaging Data Analysis: A Primer, A. Wheeler, R. Henriques, Eds. (Wiley, 2017), pp. 99–141.

70. W. J. H. Hagen, W. Wan, J. A. G. Briggs, Implementation of a cryo-electron tomography tilt-scheme optimized for high resolution subtomogram averaging. J. Struct. Biol. 197, 191–198 (2017). doi: 10.1016/j.jsb.2016.06.007; pmid: 27313000

71. R. Danev, B. Buijsse, M. Khoshouei, J. M. Plitzko, W. Baumeister, Volta potential phase plate for in-focus phase contrast transmission electron microscopy. Proc. Natl. Acad. Sci. U.S.A. 111, 15635–15640 (2014). doi: 10.1073/pnas.1418377111; pmid: 25331897

72. D. N. Mastronarde, S. R. Held, Automated tilt series alignment and tomographic reconstruction in IMOD. J. Struct. Biol. 197, 102–113 (2017). doi: 10.1016/j.jsb.2016.07.011; pmid: 27444392

73. D. N. Mastronarde, Dual-axis tomography: An approach with alignment methods that preserve resolution. J. Struct. Biol. 120, 343–352 (1997). doi: 10.1006/jsbi.1997.3919; pmid: 9441937

74. B. Turoňová, F. K. M. Schur, W. Wan, J. A. G. Briggs, Efficient 3D-CTF correction for cryo-electron tomography using NovaCTF improves subtomogram averaging resolution to 3.4 Å. J. Struct. Biol. 199, 187–195 (2017). doi: 10.1016/j.jsb.2017.07.007; pmid: 28743638

75. M. Chen et al., Convolutional neural networks for automated annotation of cellular cryo-electron tomograms. Nat. Methods 14, 983–985 (2017). doi: 10.1038/nmeth.4405; pmid: 28846087

76. A. Martinez-Sanchez, I. Garcia, S. Asano, V. Lucic, J. J. Fernandez, Robust membrane detection based on tensor voting for electron tomography. J. Struct. Biol. 186, 49–61 (2014). doi: 10.1016/j.jsb.2014.02.015; pmid: 24625523

77. B. Turoňová et al., In situ structural analysis of SARS-CoV-2 spike reveals flexibility mediated by three hinges. Science 370, 203–208 (2020). doi: 10.1126/science.abd5223

78. G. Tang et al., EMAN2: An extensible image processing suite for electron microscopy. J. Struct. Biol. 157, 38–46 (2007). doi: 10.1016/j.jsb.2006.05.009; pmid: 16859925

79. B. Turoňová et al., Benchmarking tomographic acquisition schemes for high-resolution structural biology. Nat. Commun. 11, 876 (2020). doi: 10.1038/s41467-020-14535-2; pmid: 32054835

80. S. H. W. Scheres, RELION: Implementation of a Bayesian approach to cryo-EM structure determination. J. Struct. Biol. 180, 519–530 (2012). doi: 10.1016/j.jsb.2012.09.006; pmid: 23000701

81. E. F. Pettersen et al., UCSF Chimera—A visualization system for exploratory research and analysis. J. Comput. Chem. 25, 1605–1612 (2004). doi: 10.1002/jcc.20084; pmid: 15264254

82. L. Zimmermann et al., A Completely Reimplemented MPI Bioinformatics Toolkit with a New HHpred Server at its Core. J. Mol. Biol. 430, 2237–2243 (2018). doi: 10.1016/j.jmb.2017.12.007; pmid: 29258817

83. N. Guex, M. C. Peitsch, SWISS-MODEL and the Swiss-PdbViewer: An environment for comparative protein modeling. Electrophoresis 18, 2714–2723 (1997). doi: 10.1002/elps.1150181505; pmid: 9504803

84. A. Šali, T. L. Blundell, Comparative protein modelling by satisfaction of spatial restraints. J. Mol. Biol. 234, 779–815 (1993). doi: 10.1006/jmbi.1993.1626; pmid: 8254673

85. T. Stuwe et al., Nuclear pores. Architecture of the nuclear pore complex coat. Science 347, 1148–1152 (2015). doi: 10.1126/science.aaa4136; pmid: 25745173

86. D. H. Lin et al., Architecture of the symmetric core of the nuclear pore. Science 352, aaf1015 (2016). doi: 10.1126/science.aaf1015; pmid: 27081075

87. C. S. Weirich, J. P. Erzberger, J. M. Berger, K. Weis, The N-terminal domain of Nup159 forms a β-propeller that functions in mRNA export by tethering the helicase Dbp5 to the nuclear pore. Mol. Cell 16, 749–760 (2004). doi: 10.1016/j.molcel.2004.10.032; pmid: 15574330

88. K. Yoshida, H. S. Seo, E. W. Debler, G. Blobel, A. Hoelz, Structural and functional analysis of an essential nucleoporin heterotrimer on the cytoplasmic face of the nuclear pore complex. Proc. Natl. Acad. Sci. U.S.A. 108, 16571–16576 (2011). doi: 10.1073/pnas.1112846108; pmid: 21930948

89. K. Strimmer, fdrtool: A versatile R package for estimating local and tail area-based false discovery rates. Bioinformatics 24, 1461–1462 (2008). doi: 10.1093/bioinformatics/btn209; pmid: 18441000

90. Y. Benjamini, Y. Hochberg, Controlling the false discovery rate: A practical and powerful approach to multiple testing. J. R. Stat. Soc. B 57, 289–300 (1995). doi: 10.1111/j.2517-6161.1995.tb02031.x

91. T. D. Goddard et al., UCSF ChimeraX: Meeting modern challenges in visualization and analysis. Protein Sci. 27, 14–25 (2018). doi: 10.1002/pro.3235; pmid: 28710774

92. V. Rantos, K. Karius, J. Kosinski, Integrative structural modelling of macromolecular complexes using Assembline. bioRxiv 2021.04.06.438590 [Preprint] (2021). doi: 10.1101/2021.04.06.438590

93. B. Webb et al., Integrative structure modeling with the Integrative Modeling Platform. Protein Sci. 27, 245–258 (2018). doi: 10.1002/pro.3311; pmid: 28960548

94. D. Saltzberg, C. H. Greenberg, S. Viswanath, I. Chemmama, B. Webb, R. Pellarin, I. Echeverria, A. Sali, in Biomolecular Simulations, M. Bonomi, C. Camilloni, Eds., Methods in Molecular Biology, Volume 2022 (Humana, 2019), pp. 353–377.

95. S. Viswanath, I. E. Chemmama, P. Cimermancic, A. Sali, Assessing Exhaustiveness of Stochastic Sampling for Integrative Modeling of Macromolecular Structures. Biophys. J. 113, 2344–2353 (2017). doi: 10.1016/j.bpj.2017.10.005; pmid: 29211988

96. G. Drin et al., A general amphipathic α-helical motif for sensing membrane curvature. Nat. Struct. Mol. Biol. 14, 138–146 (2007). doi: 10.1038/nsmb1194; pmid: 17220896

97. J. Kosinski et al., Data for integrative modeling of the Nuclear Pore Complex from Schizosaccharomyces pombe, Zenodo (2021). doi: 10.5281/zenodo.5585949

## ACKNOWLEDGMENTS

## SUPPLEMENTARY MATERIALS

science.org/doi/10.1126/science.abd9776
Supplementary Text
Figs. S1 to S18
Tables S1 to S4
References (98–106)
MDAR Reproducibility Checklist
Movies S1 to S7

View/request a protocol for this paper from Bio-protocol.

# Nuclear pores dilate and constrict in cellulo

Christian E. Zimmerli, Matteo Allegretti, Vasileios Rantos, Sara K. Goetz, Agnieszka Obarska-Kosinska, Ievgeniia Zagoriy, Aliaksandr Halavatyi, Gerhard Hummer, Julia Mahamid, Jan Kosinski, and Martin Beck

### Mechanosensitive nuclear pores

The nucleus of eukaryotic cells is enclosed by the nuclear envelope, a double membrane punctuated with nuclear pore complexes (NPCs). These giant channels in the nuclear envelope mediate nucleocytoplasmic exchange. Zimmerli *et al.* show that the mechanical status of the nuclear membranes controls their nuclear pore diameter. Pulling forces imposed through nuclear membranes lead to stretching of NPCs and dilation of their diameter, whereas relief of such forces causes NPC constriction. Thus, the control of nuclear size and shape is functionally linked with NPC conformation and nucleocytoplasmic transport activity. —SMH

**View the article online**
https://www.science.org/doi/10.1126/science.abd9776
**Permissions**
https://www.science.org/help/reprints-and-permissions

Use of this article is subject to the Terms of service